2017

Extraction of Displacement Fields in Heterogeneous Media Using Optimal Local Basis Functions

Paul Derek Sinz
Louisiana State University and Agricultural and Mechanical College

EXTRACTION OF DISPLACEMENT FIELDS IN HETEROGENEOUS MEDIA USING OPTIMAL LOCAL BASIS FUNCTIONS

A Dissertation

Submitted to the Graduate Faculty of the
Louisiana State University and
Agricultural and Mechanical College
in partial fulfillment of the
requirements for the degree of
Doctor of Philosophy

in

The Department of Mathematics

by
Paul Derek Sinz
B.S. in Mathematics, California Polytechnic State University, 2010
M.S. in Mathematics, Louisiana State University, 2011
August 2017

Acknowledgments

I would like to give my sincere thanks to my adviser Dr. Robert Lipton for his guidance in carrying out this work. He was a constant source of support and unwavering optimism. Thanks are also due for his providing me with the opportunities to visit and work with leaders in my research field at the University of Texas at Austin and the Air Force Research Laboratory (AFRL) in Dayton, Ohio.

I thank Dr. Ivo Babuška at the University of Texas for fruitful and enlightening conversations. I am supremely grateful for the hospitality and input from the researchers at AFRL and the University of Dayton Research Institute (UDRI) for hosting and working with me on several extended visits during the course of my graduate studies.

I would like to give particular thanks to Dr. Michael Stuebner of UDRI for his collaboration on the projects in this dissertation. Dr. Stuebner allowed me to borrow his extensive computational expertise for this work. He has been a friend and valued colleague.

Thanks to the LSU math department, from the students to the staff and faculty, for providing an excellent environment to work and study in. Thanks also to the members of my dissertation committee, Professors Mark Davidson, Richard Litherland, and Milen Yakimov.

To all my friends at LSU, thank you for all the interesting conversations and good times throughout our graduate studies.

Finally, thanks to my family for their encouragement and support in all things.

Table of Contents

Acknowledgments ii

Abstract iv

Chapter 1: Introduction 1

Chapter 2: Uncertain Loading and Energy Concentration Within Composite Structures 7
2.1 Introduction 7
2.2 Energy Concentration Inside Composite Structures 8
2.3 Energy Concentration Due to Random Boundary Data 14
2.4 Computational Approach 18
2.5 Numerical Simulations 21
2.6 Conclusions 29

Chapter 3: Implementation of Multiscale-Spectral GFEM and Optimal Oversampling 30
3.1 Introduction 30
3.2 Problem Formulation 31
3.3 Computational Method 39
3.4 Numerical Implementation for a Benchmark Problem 43
3.5 Computing Finite Dimensional Subspaces of $H_A(\omega_i^*)$ and Reduction of Computational Work 52
3.6 Contrast Independent Convergence Study 56
3.7 Conclusions 60

Chapter 4: A Two-Level Domain Decomposition Method 62
4.1 Introduction 62
4.2 Problem Formulation 62
4.3 Domain Decomposition Method Preliminaries 64
4.4 Domain Decomposition Method 67
4.5 Conclusion 72

References 74

Vita 77

Abstract

The Multiscale Spectral Generalized Finite Element Method (MS-GFEM) was developed in recent work by Babuška and Lipton. The method uses optimal local shape functions, optimal in the sense of the Kolmogorov n-width, to approximate solutions to a second order linear elliptic partial differential equation with L^∞ coefficients. In this dissertation an implementation of MS-GFEM over a two subdomain partition of unity is outlined and several numerical experiments are presented. The method is applied to compute local fields inside high contrast particle suspensions. The method's performance is evaluated for various examples with different contrasts between reinforcement particles and matrix material. The numerical experiments are shown to agree with a new theoretical estimate that shows the convergence rate is independent of the elastic properties of particles and matrix materials.

A new domain decomposition method based on MS-GFEM is presented. Numerical computations using this iterative method are discussed and the theoretical convergence rate is provided. It is shown that the convergence rate is given by the same near-exponential bound given for MS-GFEM.

A systematic method for identifying the worst case load amongst all boundary loads of a fixed energy is introduced. Here the worst case load delivers the largest fraction of input energy into a prescribed subdomain of interest. This leads to an eigenvalue problem, for which the largest eigenvalue is the maximum fraction of energy which concentrates in the subdomain. The associated eigenfunctions are the worst case solutions. These eigenfunctions are related back to the MS-GFEM shape functions and numerical results are presented for several different geometries.

Chapter 1
Introduction

The topic of this dissertation is the computation of displacement, stress, and strain fields in multiscale composite materials. To motivate the topics we focus here on carbon fiber composites. Carbon fiber composites are composed of fibers of carbon, typically 5-10μm thick, woven together in the form of a textile (just like with clothing) and embedded in another material, such as epoxy resin. Due to their high level of strength relative to weight, carbon fiber composites have become a popular structural material amongst airplane manufacturers as well as car and ship manufacturers. The Boeing 787 Dreamliner, for example, is composed of 50% carbon fiber composites by weight (www.Boeing.com). Knowledge of the stress and strain fields within a material (internal forces and deformations) is used to predict where damage may occur when the material is subjected to external forces. There is an increasing demand for the numerical simulation of these fields in science and industry to mitigate the costs of experiments and to aid in design and analysis. The computation of these fields within carbon fiber composites is dependent upon several different length scales, starting from the scale of the fibers themselves, to the next level of the weave and layout of the fibers, up to the layering of plies, and so on up to the length scale of, for instance, an airplane wing. The multiscale nature of the problem makes the numerical computations challenging and expensive as each length scale must be resolved in the model resulting in a large number of degrees of freedom.

The linear elliptic partial differential equation modeling infinitesimal strain linear elasticity in a body $\Omega \subset \mathbb{R}^d$, $d = 2, 3$, with displacement $u(x) \in \mathbb{R}^d$ is given

by

$$-\operatorname{div}(\mathbb{A}(x)\nabla u(x)) = f(x) \text{ in } \Omega \tag{1.1}$$

for $\mathbb{A}$ the symmetric tensor of elasticity and $f(x)$ a body force with Dirichlet boundary data

$$u(x) = h(x) \text{ in } \Gamma_D \subset \partial\Omega \tag{1.2}$$

or Neumann boundary data

$$n \cdot \mathbb{A}\nabla u = g(x) \text{ in } \Gamma_N \subset \Omega. \tag{1.3}$$

The solution u is sought in the Sobolev space $H^1(\Omega)$ through the weak formulation of the above equations. In this work we study and implement the recently introduced Multiscale Spectral Generalized Finite Element Method (MS-GFEM). We implement the method using a partition of unity with two subdomains in the context of the two-dimensional conductivity problem assuming knowledge of the material properties $\mathbb{A}(x)$ throughout the material domain Ω. This work has been carried out in collaboration with Michael Stuebner of the University of Dayton Research Institute, Robert Lipton of Louisiana State University, and Ivo Babuška of the University of Texas at Austin.

One of the most popular methods of computing stress and strain fields is the celebrated Finite Element Method (FEM). In FEM, a set of prescribed functions called shape functions is used to approximate the actual fields. This allows for simple computations using classical linear algebra techniques. The drawback is that the computation is only as good as the given shape functions, that is, the FEM is limited to approximating the behavior that is modeled well by the shape functions. The practitioner is left to choose the appropriate FEM with specified shape functions.

The Generalized Finite Element Method (GFEM) is an attempt at relieving this drawback while maintaining the usage of simple linear algebra techniques. GFEM allows specific knowledge of the problem at hand to be used to choose shape functions with greater approximation capabilities in different regions of the material. This can result in the reduction in problem size by reducing the number of degrees of freedom in the problem for achieving a desired level of accuracy. The MS-GFEM is a GFEM with a particular choice of shape functions.

The GFEM is a type of partition of unity method (PUM), in which the problem domain Ω is separated into overlapping subdomains $\Omega = \cup_{i=1}^{N} \omega_i$. On each subdomain local shape functions may be selected and recombined using a partition of unity over the subdomains to create global shape functions. The PUM was developed by Melenk and Babuska [27] and uses the partition of unity concept to introduce enrichment functions into local approximation spaces for the solution of partial differential equations. The GFEM, also called the extended finite element method (XFEM), uses traditional FEM techniques while alleviating several challenges in FEM by allowing for the use of typical finite element shape functions while also allowing for the enrichment of the approximation space with shape functions for the specific problem at hand. These enrichment functions could contain information about the local microstructure and material properties or of cracks and defects in the material. For example, the Heaviside step function is frequently used to model a crack. A mathematical survey of GFEM is given in [2] and a review of the method for material modeling is given in [4]. These works also contain large lists of references detailing the historical development of GFEM.

The ability of GFEM to include a multitude of enrichment functions introduces a new problem; which enrichment functions are the best for the problem at hand? In [33], several specific handbook functions are computed for local geometries con-

taining inclusions and cracks. These handbook functions are used as the local enrichment functions. A different approach is taken in the development of MS-GFEM in [6] and [5], in which the shape functions are computed for the problem at hand through oversampling over the subdomains. Here oversampling refers to selecting functions over extended subdomains $\omega_i^* \supset \omega_i$ and restricting them to ω_i. This approach is motivated by the Cacciopoli inequality and St. Venant's principle, which roughly stated says that the difference in the effects of two different but statically equivalent loads becomes small away from where the load is applied. This oversampling results in optimal local shape functions in the sense of the Kolmogorov n-width. The formulation of the oversampling problem with n-widths results in a spectral problem, with the associated eigenfunctions of this spectral problem being the optimal local shape functions used in MS-GFEM. These local shape functions display exponential convergence properties with the associated eigenvalues bounding the local and global errors.

In chapter 2 of this dissertation an alternate motivation for the shape function of MS-GFEM is found through the study of a worst case loading problem. It is a natural question to ask how much elastic energy will concentrate in a given subdomain of interest within a material. To illustrate this idea, consider an airplane wing. When subjected to a critical load, damage is likely to begin near a structural feature such as a bolt hole. Knowledge of how much elastic energy will concentrate in this subdomain of interest is required. Here the subdomain of interest is the region of the wing around the bolt hole and the elastic energy that concentrates in this domain is the product of the stress and strain fields within the domain. Further complicating the matter is that the actual loads a wing is subjected to have a random nature (varying wind patterns, for instance). Thus, we arrive at the problem of determining which boundary load, amongst all possible loads, con-

centrates the most elastic energy in the subdomain of interest. This boundary load is identified as the worst case boundary load.

Rather than directly identifying the worst case boundary load, we can instead identify the worst case solution of the underlying partial differential equation associated to that boundary load. We take the worst case solution as that which maximizes the fraction of elastic energy in the subdomain of interest. The variational formulation of this problem is to find a stationary point $\tilde{u}$ and value V such that

$$V = \sup \left\{ \frac{\|u\|^2_{\mathcal{E}(\omega)}}{\|u\|^2_{\mathcal{E}(\Omega)}} \ : \ \mathrm{div}\left(\mathbb{A}(x)\nabla u(x)\right) = 0 \right\} \tag{1.4}$$

with ω the subdomain of interest within the material domain Ω. In chapter 2 the solution to this problem is presented in Theorems 2.1 and 2.3 for Dirichlet and Neumann boundary conditions, respectively. There it is seen that this worst case load is none other than the first eigenvalue-eigenfunction pair corresponding to the spectral problem from MS-GFEM. Therefore, we see that the use of these optimal local shape functions are physically motivated by being the functions which concentrate elastic fields within a subdomain. Restricting these functions to the subdomain results in shape functions which carry a maximal amount of information about the local fields, making them an obvious candidate for usage as local shape function in the context of a GFEM. These theoretical results are supported with numerical simulations for several domains with circular inclusions and holes.

In chapter 3 a full numerical implementation of MS-GFEM is presented along with numerical results for a model problem. A convergence study is presented which compares the rate of convergence of solutions with respect to the number of local shape functions used with varying contrasts between material properties. Computations are carried out for a large range of contrast between particle and matrix conductivities. The matrix material refers to the material in which the particles

are embedded. For inclusions that do not touch and have smooth boundary our computations show that the MS-GFEM approximations converge exponentially independently of the elastic contrast between phases. This is consistent with the simulations for scalar problems given in [33] for a medium with separated holes. This is also consistent with the more recent numerical investigation carried out for scalar and elastic problems using the optimal local basis functions in [30]. In computing the optimal local shape functions a spectral problem on each subdomain ω_i must be constructed and solved. All computations are independent and may be performed in parallel, however this still presents a large computational cost. A method to reduce the cost of generating local basis functions is presented and it is shown that this method retains accuracy while reducing the computational work necessary to generate local bases.

The present work is completed in chapter 4 in which a two-level domain decomposition method using the optimal local shape functions of MS-GFEM is presented. The method is presented for the iterative solution of the conductivity problem with Neumann boundary conditions. An exponential convergence estimate for the method is provided and proven. The proof utilizes the exponential convergence estimate of MS-GFEM proven in [6]. This iterative method is placed in the context of domain decomposition methods, see [36] and [31] for an introduction and references. This iterative method leverages all the computations performed during a run of the MS-GFEM algorithm to iterate the solution and increase its accuracy geometrically in terms of the MS-GFEM exponential bounds. It is anticipated that this will allow for a reduction in the number of optimal local shape functions required to compute for achieving a desired numerical accuracy.

Chapter 2

Uncertain Loading and Energy Concentration Within Composite Structures

2.1 Introduction

Composite materials often fail near structural features where stress can concentrate. Examples include neighborhoods surrounding lap joints or bolt holes where composite structures are fastened or joined [34]. Large boundary loads deliver energy to the structure and can increase the overall energy near structural features and initiate failure. These considerations provide motivation for a better understanding of energy penetration and concentration inside structures associated with boundary loading. One possible approach is to apply the Saint-Venant principle [29], [25], [35], [26] to characterize the rate of decay of the magnitude of the stress or strain away from the boundary and study its effect on interior subdomains. This type of approach provides theoretical insight for homogeneous materials. However for composite structures the decay can be slow and far from exponentially decreasing away from the boundary [17]. With this in mind we attempt a more refined analysis and address the problem from an energy based perspective. In this chapter we examine the proportion of the total energy that is contained within a prescribed interior domain of interest in response to boundary displacements or traction loads imposed on the composite structure.

We introduce a computational method for identifying the worst case load defined to be the one that delivers the largest portion of a given input energy to a prescribed interior domain of interest. The interior domain ω can surround bolted or bonded joints where stress can concentrate. Here the interior domain is taken to be a positive distance away from the part of the external boundary of the structural

domain ω^* where the loads are applied. We show here that it is possible to quantify the effects of a worst case load that concentrates the greatest proportion of energy onto ω by a suitably defined *concentration* eigenvalue problem. The largest eigenvalue for the eigenvalue problem is equal to the maximum fraction of total elastic energy that can be imparted to the subdomain over all boundary loads. The displacement field associated with the worst case load is the eigenfunction associated with the largest eigenvalue. This eigenvalue problem is related to the eigenvalue problems associated with finding the optimal local basis, see [6], [5]. This is also related to the notion of the penetration function and best choice of optimal basis introduced in [7].

As an application we use the concentration eigenvalue problem to bound the fraction of energy imparted on a prescribed subdomain by the worst case load associated with an ensemble of random loads. While it is possible to consider any type of random boundary loading we illustrate the ideas for boundary loads described by a second order random process specified in terms of its covariance function and ensemble average.

We conclude noting that related earlier work provides bounds on the local stress and strain amplification generated by material microstructure. Of interest is to identify minimum stress microstructures with the lowest field amplification over all microstructures [1], [10]. These results enable the design of graded microstructures for suppression of local stress inside structural components [20], [22].

2.2 Energy Concentration Inside Composite Structures

In this section we develop the notion of energy penetration and its associated concentration within a composite structure. The structural domain ω^* is made of a composite material and described by the elastic tensor $\mathbb{A}(x)$ taking different values inside each component material. The composite structures addressed here

are general and include fiber reinforced laminates or particle reinforced composites. We suppose that the composite structure is subjected to an ensemble of boundary loads applied to either part or to all of the boundary of the structural domain ω^*. We are interested in the energy concentration around features such as a bolt holes or lap joints contained within a known subdomain ω of the structural domain ω^*. Here it is assumed that the boundary of the subdomain ω is of positive distance away from the part of the structural boundary where loads are being applied.

The notion of energy concentration applies to both Dirichlet and traction boundary loading. To fix ideas we first consider Dirichlet loading. The elastic displacement u is assigned the Dirichlet data g on the exterior boundary of the domain ω^* denoted by $\partial\omega^*$. The structural domain ω^* may be taken to be a bracket or fastener and contain bolt holes away from the exterior boundary where loads are applied. The boundaries of these holes are assumed clamped and have zero elastic displacement. The collection of these interior boundaries is denoted by $\partial\omega_I^*$, see Figure 2.1. The elastic displacement is the solution of the linear elastic system inside the structural domain ω^* given by

$$\operatorname{div}\left(\mathbb{A}(x)e(u(x))\right) = 0, \tag{2.1}$$

where $e(u(x))$ is the elastic strain $e(u(x)) = (\nabla u(x) + \nabla u(x)^T)/2$ and the elasticity tensor $\mathbb{A}$ satisfies the standard ellipticity and boundedness conditions:

$$\lambda|\zeta|^2 \leq \mathbb{A}(x)\zeta : \zeta \leq \Lambda|\zeta|^2, \tag{2.2}$$

where ζ is any constant strain tensor, $0 < \lambda < \Lambda$ and $\mathbb{A}(x)\zeta : \zeta$ is the elastic energy density given by

$$\mathbb{A}(x)\zeta : \zeta = \sum_{ijkl} \mathbb{A}_{ijkl}(x)\zeta_{kl}\zeta_{ij} \tag{2.3}$$

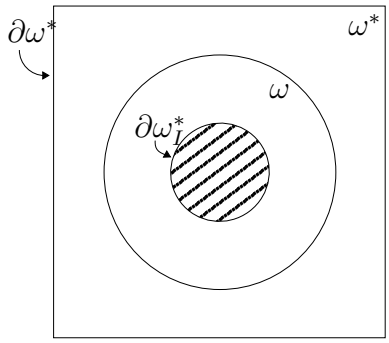

FIGURE 2.1: Boundary $\partial\omega^*$ and interior domain ω surrounding bolt hole.

The work done on the boundary $\partial\omega^*$ delivers the total elastic energy inside the structure and is given by

$$E(g) = \int_{\partial\omega^*} \mathbb{A}e(u)n \cdot g \, ds = \int_{\omega^*} \mathbb{A}e(u) : e(u) \, dx, \tag{2.4}$$

where n is the outward pointing unit normal and $\mathbb{A}e(u)n$ is the traction and g is the boundary displacement.

Now fix a subdomain ω of interest with boundary a positive distance away from the structural boundary subjected to loading. Here the domain ω can be selected to contain a bolt hole or other interior feature of the structure, see Figure 2.1. The elastic energy inside this subdomain is written

$$(u, u)_{\mathcal{E}(\omega)} = \int_{\omega} \mathbb{A}(x)e(u) : e(u) \, dx, \tag{2.5}$$

and the total elastic energy in the structure is written

$$(u, u)_{\mathcal{E}(\omega^*)} = \int_{\omega^*} \mathbb{A}e(u) : e(u) \, dx. \tag{2.6}$$

The energy norms for the subdomain and structure are written as

$$\|u\|^2_{\mathcal{E}(\omega)} = (u, u)_{\mathcal{E}(\omega)} \tag{2.7}$$

and

$$\|u\|^2_{\mathcal{E}(\omega^*)} = (u, u)_{\mathcal{E}(\omega^*)} = E(g). \tag{2.8}$$

and the fraction of the total elastic energy in the structure that is contained inside the subdomain ω is given by the ratio

$$P(g) = \frac{\|u\|^2_{\mathcal{E}(\omega)}}{E(g)} = \frac{\|u\|^2_{\mathcal{E}(\omega)}}{\|u\|^2_{\mathcal{E}(\omega^*)}}. \tag{2.9}$$

We define $P(g)$ to be the energy concentration function associated with the boundary displacement g. Collecting our observations we have

$$P(g) = \frac{\|u\|^2_{\mathcal{E}(\omega)}}{\|u\|^2_{\mathcal{E}(\omega^*)}} \ : \ \text{with } \operatorname{div}(\mathbb{A}(x)e(u(x))) = 0 \text{ and } u = g \text{ on } \partial\omega^* \ . \tag{2.10}$$

We proceed to identify the worst case displacement over all boundary data g associated with solutions of the elastic system that have square integrable displacements and strain tensors on ω^*. On the interior boundary $\partial\omega^*_I$ we assume clamped boundary conditions for the elastic displacement. We denote this space of displacements by $H^1_{I0}(\omega^*)$ and the associated boundary displacements on $\partial\omega^*$ reside in the space $H^{1/2}(\partial\omega^*)$. It is well known that each boundary displacement in $H^{1/2}(\partial\omega^*)$ corresponds to a unique solution u of the elastic system in $H^1_{I0}(\omega^*)$, see [15]. Conversely every solution u of the elastic system in $H^1_{I0}(\omega^*)$ has boundary values in $H^{1/2}(\partial\omega^*)$. The worst case displacement $\tilde{g}$ on $\partial\omega^*$ for the domain ω delivers the maximum energy concentration

$$P(\tilde{g}) = \max\left\{P(g) \ : \ g \text{ in } H^{1/2}(\partial\omega^*)\right\}. \tag{2.11}$$

We now state the theorem which identifies the worst case displacement $\tilde{g}$ in $H^{1/2}(\partial\omega^*)$.

Theorem 2.1. *The variational problem given by*

$$V = \sup\left\{ \frac{\|u\|^2_{\mathcal{E}(\omega)}}{\|u\|^2_{\mathcal{E}(\omega^*)}} \ : \ u \text{ in } H^1_{I0}(\omega^*) \text{ with } \operatorname{div}(\mathbb{A}(x)e(u(x))) = 0 \right\} \tag{2.12}$$

has a maximum $\tilde{u}$ and the maximum energy concentration inside ω is given by

$$V = P(\tilde{g}) = \max\left\{P(g) \ : \ g \text{ in } H^{1/2}(\partial\omega^*)\right\}. \tag{2.13}$$

where the worst case displacement is given by the boundary value of $\tilde{u}$ *on* $\partial\omega^*$*. Moreover, the stationary point* $\tilde{u}$ *and stationary value* V *are identified as the eigenfunction eigenvalue pair associated with the solution to the penetration eigenvalue problem given by:*

Find u *and* λ *for which* u *belongs to* $H^1_{I0}(\omega^*)$ *and is a solution of*

$$\operatorname{div}(\mathbb{A}(x)e(u(x))) = 0, \text{ for } x \text{ in } \omega^*, \tag{2.14}$$

and

$$\lambda(u,v)_{\mathcal{E}(\omega^*)} = (u,v)_{\mathcal{E}(\omega)} \tag{2.15}$$

for all trial fields v *belonging to* $H^1_{I0}(\omega^*)$ *that satisfy* $\operatorname{div}(\mathbb{A}(x)e(v(x))) = 0$.

Remark 2.2. *The maximum* $\tilde{u}$ *may not be unique. If the eigenspace corresponding to the largest eigenvalue of* (2.15) *has dimension greater than 1, then the maximum* V *is attained by any vector* u *in this eigenspace.*

It is clear from the formulation that V does not depend on boundary load but is instead dependent only on the geometry of the boundary of the specimen ω^*, the shape and location of ω, and the microstructure associated with the composite material contained inside the structure. A simple example illustrating the nature of V is given by the anti-plane shear problem associated with a homogeneous prismatic shaft with circular cross-section ω^* of radius 1. The shaft is made from homogeneous isotropic elastic material with specified shear and bulk moduli. On choosing ω to be a disk of radius r centered inside ω^* a simple calculation shows that $V = r$. What is notable is that the maximum fraction of energy that can be delivered to ω scales as r as opposed to the area fraction of the disk which scales as r^2.

Next we consider the computation of the worst case traction load and its associated energy concentration. Traction loading $t = \mathbb{A}e(u)n$ is applied to the boundary

of the domain $\partial\omega^*$ and the elastic displacement is the solution of the linear elastic system inside the structural domain ω^* given by

$$\operatorname{div}\left(\mathbb{A}(x)e(u(x))\right) = 0. \tag{2.16}$$

For this case one considers all traction loads t belonging to the space $H^{-1/2}(\partial\omega^*)$. This space corresponds to all traction boundary values associated with $H^1_{I0}(\omega^*)$ solutions of (2.16). The work done against the applied traction t is equal to the total elastic energy and we write

$$E(t) = \int_{\partial\omega^*} t \cdot u ds = \int_{\omega^*} \mathbb{A}e(u) : e(u)\, dx = \|u\|^2_{\mathcal{E}(\omega^*)}. \tag{2.17}$$

The fraction of the total elastic energy in the structure that is contained inside the subdomain ω is given by the ratio

$$P(t) = \frac{\|u\|^2_{\mathcal{E}(\omega)}}{E(t)} = \frac{\|u\|^2_{\mathcal{E}(\omega)}}{\|u\|^2_{\mathcal{E}(\omega^*)}}. \tag{2.18}$$

Here we refer to $P(t)$ as the energy concentration function associated with the boundary traction t. The maximum energy concentration inside ω is given by

$$P(\tilde{t}) = \max\left\{P(t) \,:\, t \text{ in } H^{-1/2}(\partial\omega^*)\right\} \tag{2.19}$$

We now proceed as before and state the theorem which identifies the worst case traction $\tilde{t}$ in $H^{-1/2}(\partial\omega^*)$.

Theorem 2.3. *The variational problem given by*

$$V = \sup\left\{ \frac{\|u\|^2_{\mathcal{E}(\omega)}}{\|u\|^2_{\mathcal{E}(\omega^*)}} \,:\, u \text{ in } H^1_{I0}(\omega^*) \text{ with } \operatorname{div}\left(\mathbb{A}(x)e(u(x))\right) = 0 \right\} \tag{2.20}$$

has a maximum $\tilde{u}$ and the maximum energy concentration inside ω is given by

$$V = P(\tilde{t}) = \max\left\{P(t) \,:\, t \text{ in } H^{-1/2}(\partial\omega^*)\right\} \tag{2.21}$$

and the worst case traction is given by $\mathbb{A}e(\tilde{u})n$ on $\partial\omega^*$.

Moreover the maximizer $\tilde{u}$ and V are the same eigenfunction eigenvalue pair associated with the solution to the concentration eigenvalue problem (2.15).

Remark 2.4. *It is important to note that Theorems 2.1 and 2.3 apply to the concentration of energy inside ω associated with work done on the boundary so $\tilde{u}$ and V are the same for the cases of applied traction and applied displacement.*

In this chapter we will compute the worst case boundary loads and associated maximum energy concentration through the numerical solution of the concentration eigenvalue problem (2.15). Theorems 2.1 and 2.3 identify the space of test and trial functions for use in the computation of the maximum energy concentration V and associated elastic field $\tilde{u}$. This space is denoted by $H_{\mathbb{A}}(\omega^*)$ and is the space of all functions belonging to $H^1_{I0}(\omega^*)$ that are solutions of $\text{div}(\mathbb{A}e(u)) = 0$. In Section 2.4 we provide a numerical method for computing the maximum energy concentration and worst case load by finding u in $H_{\mathbb{A}}(\omega^*)$ and λ for which

$$\lambda(u, v)_{\mathcal{E}(\omega^*)} = (u, v)_{\mathcal{E}(\omega)}. \tag{2.22}$$

for all trial fields v belong to $H_{\mathbb{A}}(\omega^*)$.

Remark 2.5. *We conclude noting that the concentration eigenvalue problem* (2.22) *corresponds to the largest singular value of the restriction operator $\mathcal{P}$ defined by $\mathcal{P}(u) = u$ for x in ω where $\mathcal{P}$ acts on the space $H_{\mathbb{A}}(\omega^*)$, see [6] and [5]. It is shown there that the associated set of singular values decay nearly exponentially and that the associated eigenfunctions of $\mathcal{P}^*\mathcal{P}$ are a complete orthogonal system for the the space $H_{\mathbb{A}}(\omega^*)$.*

2.3 Energy Concentration Due to Random Boundary Data

In this section we introduce random loading on the boundary of the domain ω^* and describe the expected value of the energy concentration associated with the ensemble of random loads. We show that this quantity is bounded above by the

maximum energy concentration obtained through the solution of the eigenvalue problem (2.22). It is possible to consider any type of random boundary loading; however, to fix ideas we assume in this treatment that the loading is a second order random process with specified covariance and expectation. In what follows we apply the Kosambi-Karhunen-Loeve (KKL) expansion (cf. [14]) of the random boundary displacement, g with average, $\bar{g}(x)$, and mean zero fluctuation, $\alpha(x,\theta)$, as

$$g(x,\theta) = \bar{g}(x) + \alpha(x,\theta). \tag{2.23}$$

We assume, with no loss of generality, that $\bar{g}(x)$ and $\alpha(x,\theta)$ belong to $H^{1/2}(\partial\omega^*)$. Where $\alpha(x,\theta)$ is a zero mean, second order stochastic process with covariance function $C(x_1,x_2)$ defined for points x_1 and x_2 on $\partial\omega^*$. The corresponding KKL expansion of $g(x,\theta)$ is given by

$$g(x,\theta) = \bar{g}(x) + \sum_{n=0}^{\infty} \sqrt{\mu_n}\psi_n(\theta)\tilde{g}_n(x) \tag{2.24}$$

where the deterministic functions $\tilde{g}_n(x)$ and parameters μ_n are the eigenfunctions and eigenvalues of the integral equation

$$\int_{\partial\omega^*} C(x_1,x)\hat{g}_n(x,\theta)\,ds = \mu_n\hat{g}_n(x_1,\theta), \text{ for } x_1 \text{ on } \partial\omega^*, \tag{2.25}$$

where ds is the surface measure with respect to the x variable. The mean zero random variables, $\psi_n(\theta)$, are determined by

$$\psi_n(\theta) = \frac{1}{\sqrt{\mu_n}} \int_{\partial\omega^*} \alpha(x,\theta)\hat{g}_n(x)\,ds \tag{2.26}$$

and the functions $\psi_n(\theta)$ and $\hat{g}_n(x)$ satisfy the orthonormality conditions

$$\langle \psi_m(\theta)\psi_n(\theta)\rangle = \delta_{mn} \tag{2.27}$$

$$\int_{\partial\omega^*} \hat{g}_m(x)\cdot\hat{g}_m(x)\,ds = \delta_{mn} \tag{2.28}$$

for the Kronecker delta function, δ_{mn}, and expectation value, $\langle\cdot\rangle$. The set of all random boundary conditions $g(x,\theta)$ associated with mean $\bar{g}(x)$ and covariance $C(x_1,x_2)$ is denoted by $\mathcal{R}(\partial\omega^*)$. Using the KKL expansion (2.24) in (2.1), and by linearity, we have an expansion of the solution

$$u(x,\theta) = \bar{u}(x) + \sum_{n=0}^{\infty} \sqrt{\mu_n}\psi_n(\theta)\hat{u}_n(x) \tag{2.29}$$

where $\bar{u}(x)$ is the solution of

$$\begin{cases} \operatorname{div} \mathbb{A}e\bar{u} = 0 & \text{in } \omega^* \\ \bar{u} = \bar{g} & \text{on } \partial\omega^* \end{cases} \tag{2.30}$$

and $\hat{u}_n(x,\theta)$ is the solution of

$$\begin{cases} \operatorname{div} \mathbb{A}e\hat{u}_n = 0 & \text{in } \omega^* \\ \hat{u}_n = \hat{g_n} & \text{on } \partial\omega^* \end{cases} \tag{2.31}$$

Then $\bar{u}(x)$ is the displacement due to the ensemble average boundary data, $\bar{g}(x)$, and

$$\sum_{n=0}^{\infty} \sqrt{\mu_n}\psi_n(\theta)\hat{u}_n(x) \tag{2.32}$$

is the displacement due to the random fluctuations in the boundary data. The boundary data is approximated by truncating (2.24) after N terms giving the approximate solution

$$u_N(x,\theta) = \bar{u}(x) + \sum_{n=0}^{N} \sqrt{\mu_n}\psi_n(\theta)\hat{u}_n(x) \tag{2.33}$$

The expectation value of the energy of u over ω^* is denoted by $\mathcal{E}(\omega^*)$. For this case we apply the orthonormality condition (2.27) to get

$$\mathcal{E}(\omega^*) = \left\langle (u,u)_{\mathcal{E}(\omega^*)} \right\rangle = \|\bar{u}\|^2_{\mathcal{E}(\omega^*)} + \sum_{n=0}^{\infty} \mu_n \|\hat{u}_n\|^2_{\mathcal{E}(\omega^*)} \tag{2.34}$$

Truncating the sum after N terms gives the approximation u_N and the approximate expected value of the energy is given by

$$\mathcal{E}_N(\omega^*) = \|\bar{u}\|^2_{\mathcal{E}(\omega^*)} + \sum_{n=0}^{N} \mu_n \|\hat{u}_n\|^2_{\mathcal{E}(\omega^*)} \tag{2.35}$$

The expected value of the energy, $\mathcal{E}(\omega)$, which concentrates within the domain of interest, ω, is defined

$$\mathcal{E}(\omega) = \left\langle (u,u)_{\mathcal{E}(\omega)} \right\rangle = \|\bar{u}\|^2_{\mathcal{E}(\omega)} + \sum_{n=0}^{\infty} \mu_n \|\hat{u}_n\|^2_{\mathcal{E}(\omega)} \tag{2.36}$$

with truncation

$$\mathcal{E}_N(\omega) = \left\langle (u_N,u_N)_{\mathcal{E}(\omega)} \right\rangle = \|\bar{u}\|^2_{\mathcal{E}(\omega)} + \sum_{n=0}^{N} \mu_n \|\hat{u}_n\|^2_{\mathcal{E}(\omega)}, \tag{2.37}$$

where the orthogonality conditions (2.27) are used to obtain the right most equalities. The ratio

$$\overline{P} = \frac{\mathcal{E}(\omega)}{\mathcal{E}(\omega^*)} \tag{2.38}$$

is a measure of the expected proportion of energy that is contained within the domain of interest, ω, due to the random boundary conditions. Its truncation $\overline{P}_N$ is defined by

$$\overline{P}_N = \frac{\mathcal{E}_N(\omega)}{\mathcal{E}_N(\omega^*)}. \tag{2.39}$$

We now consider the maximum energy concentration $P(\mathcal{R})$ into the subdomain ω associated with the worst possible load $g(x,\theta)$ in $\mathcal{R}(\omega^*)$. The maximum energy concentration is defined as

$$P(\mathcal{R}) = \max\left\{P(g) \,:\, g = g(x,\theta) \text{ in } \mathcal{R}(\partial\omega^*)\right\} \tag{2.40}$$

where $P(g)$ is the energy concentration associated with the boundary displacement given by (2.10). It is evident from Theorem 2.1 that we have the inequalities

$$\overline{P} \le P(\mathcal{R}) \le V. \tag{2.41}$$

From the definition of $P(\mathcal{R})$ we have

$$\|u\|^2_{\mathcal{E}(\omega)} \leq P(\mathcal{R})\|u\|^2_{\mathcal{E}(\omega^*)}. \tag{2.42}$$

Applying the expectation $\langle \cdot, \cdot \rangle$ the first inequality in (2.41) follows.

In the following sections we obtain bounds on the maximum energy concentration $P(\mathcal{R})$ by computing V. The maximum energy concentration V is computed through the solution of the eigenvalue problem (2.22). In Section 2.5 we compare computed values of the expected energy concentration $\overline{P}$ with the computed values of V for different structural components made from reinforced composite materials.

2.4 Computational Approach

In this section we outline our method for computing the expected energy concentration $\overline{P}$ associated with random boundary loading as well as the computation of the maximum energy concentration V through the solution of the eigenvalue problem (2.22). We illustrate the method for the antiplane shear problem. For this case u is the out of plane displacement inside a long prismatic shaft and ω^* is the shaft cross-section. For the purpose of computation we consider polygonal domains ω^*. The out of plane deformation u is the solution of

$$\begin{cases} \text{div}\,(c(x)\nabla u(x,\theta)) = 0 \text{ in } \omega^* \\ u(x,\theta) = g(x,\theta) \text{ on } \partial\omega^* \\ u(x,\theta) = 0 \text{ on } \partial\omega^*_I \end{cases} \tag{2.43}$$

where the coefficient $c(x)$ is the shear modulus taking different values inside each component material. From (2.24) the random boundary displacement is given by $u(x,\theta) = \bar{g}(x) + g(x,\theta)$ with

$$g(x,\theta) = \sum_{n=0}^{\infty} \sqrt{\mu_n}\psi_n(\theta)\hat{g}_n(x) \tag{2.44}$$

and we choose the Markovian covariance function

$$C(x_1, x_2) = e^{-|x_1 - x_2|/b} \tag{2.45}$$

where b is the correlation length with the same units as x. The domain of interest ω has boundary a positive distance away from $\partial\omega^*$. Closed form solutions for the sequence $\{\hat{g}_n\}_{n=1}^{\infty}$ appearing in (2.44) are obtained through the solution of

$$\int_{-a}^{a} C(x, x_1)\hat{g}_n(x, \theta)\, dx = \mu_n \hat{g}_n(x_1, \theta), \text{ for } x_1 \text{ on } (-a, a), \tag{2.46}$$

as in [14, page 31] and given by

$$\begin{aligned} \hat{g}_n(x) &= \frac{\cos(\gamma_n x)}{\sqrt{a + \frac{\sin(\gamma_n)}{2\gamma_n}}}, \quad \mu_n = \frac{2c}{\gamma_n^2 + c^2} \\ \hat{g}'_n(x) &= \frac{\sin(\gamma'_n x)}{\sqrt{a - \frac{\sin(\gamma'_n)}{2\gamma'_n}}}, \quad \mu'_n = \frac{2c}{\gamma'^2_n + c^2} \end{aligned} \tag{2.47}$$

where $c = 1/b$ and $\gamma_n, \gamma'_n \geq 0$ are solutions to the equations

$$\begin{cases} c - \gamma \tan(\gamma a) = 0 \\ \gamma' + c \tan(\gamma a) = 0. \end{cases} \tag{2.48}$$

The random boundary data on $\partial\omega^*$ is provided by mapping the one dimensional KKL solutions (2.47) defined on the interval $(-a, a)$ onto the boundary of ω^*. The expected energy concentration $\overline{P}$ is given by

$$\overline{P} = \frac{\|\bar{u}\|^2_{\mathcal{E}(\omega)} + \sum_{n=0}^{\infty} \mu_n \|\hat{u}_n\|^2_{\mathcal{E}(\omega)}}{\|\bar{u}\|^2_{\mathcal{E}(\omega^*)} + \sum_{n=0}^{\infty} \mu_n \|\hat{u}_n\|^2_{\mathcal{E}(\omega^*)}}, \tag{2.49}$$

where $\hat{u}_n$ and $\hat{u}'_n$ are the solutions to (2.43) with mapped boundary data $\hat{g}_n$ and $\hat{g}'_n$, respectively. In the simulations we apply the standard finite element method to calculate the expected energy concentration truncated after N terms given by

$$\overline{P}_N = \frac{\|\bar{u}\|^2_{\mathcal{E}(\omega)} + \sum_{n=0}^{N} \mu_n \|\hat{u}_n\|^2_{\mathcal{E}(\omega)}}{\|\bar{u}\|^2_{\mathcal{E}(\omega^*)} + \sum_{n=0}^{N} \mu_n \|\hat{u}_n\|^2_{\mathcal{E}(\omega^*)}}. \tag{2.50}$$

Next we outline the strategy for numerical solution of the eigenvalue problem (2.22).

1. In the first step we build a suitably large finite dimensional subspace of $H_{\mathbb{A}}(\omega^*)$. An n-dimensional basis $\{\psi_1, \psi_2, \ldots, \psi_n\}$ of discreet solutions to

$$\operatorname{div}(c(x)\nabla u(x)) = 0 \text{ for } x \text{ in } \omega^*$$

is generated from FE solutions associated with a suitable n-dimensional set of linearly independent boundary data posed over $\partial\omega^*$. Here the n-dimensional basis of boundary data is generated by hat functions supported on $\partial\omega^*$. On the interior boundary $\partial\omega_I^*$ the discrete solutions satisfy the clamped boundary condition $u = 0$.

2. The second step is to employ the n-dimensional basis of discrete solutions as n-dimensional test and trial spaces in the finite dimensional discretization of the eigenvalue problem (2.22). This delivers the finite dimensional generalized eigenvalue problem

$$\lambda A\overline{x} = B\overline{x},$$

where $\overline{x}$ is the coordinate vector associated with the basis $\{\psi_1, \psi_2, \ldots, \psi_n\}$ and the stiffness matrices are given by

$$A_{ij} = (\psi_i, \psi_j)_{\mathcal{E}(\omega^*)} \text{ and } B_{ij} = (\psi_i, \psi_j)_{\mathcal{E}(\omega)}.$$

3. The third step solves the generalized eigenvalue problem using standard procedures. Since the matrix A is symmetric and positive definite we apply a Cholesky factorization, $A = U^T U$, where U is an upper triangular matrix. Then we write the generalized problem as a standard eigenvalue problem $C\overline{y} = \lambda\overline{y}$ where $C = (U^T)^{-1} B U^{-1}$ and $\overline{y} = U\overline{x}$. This problem is solved using a divide-and-conquer eigenvalue algorithm. The eigenvalues of the standard problem are the same as for the general problem. The eigenvectors $\overline{x}$ are com-

puted by solving $U\overline{x} = \overline{y}$. For all operations routines from the Intel Math Kernel Library [19] are used.

The associated eigenfunction $\tilde{u}_n(x) = \sum_{i=1}^{n} x_i \psi_i(x)$ and eigenvalue $\lambda = V$ deliver the numerical approximation of the worst case load and the maximum energy concentration inside ω.

2.5 Numerical Simulations

We carry out numerical approximations of the expected energy concentration $\bar{P}_N$ and the worst case energy concentration V for (2.43) over four different geometries with Dirichlet boundary conditions. For each geometry we specify the parameters a, b, and $c(x)$ and follow the procedures laid out in Section 2.4. The parameter a defines the one dimensional domain of the random boundary loads which are mapped to the boundary of each geometry, so a is half the perimeter of the geometry. Each geometry is defined by a cross-sectional area with a hole and several heterogeneities. The geometries are defined below in Sections 2.5.1-2.5.4. The geometries and the average ensemble load are displayed in Figures 2.2a-2.5a. The computational results for each geometry are displayed in Figures 2.6-2.9. All fields portrayed are normalized by the square root of the work done at the boundary of each geometry. Table 2.1 shows the computed values of V and $\bar{P}_N$ for each geometry as well as the number of functions from the KKL expansion for $g(x, \theta)$ that are used. All units are dimensionless. Mixed quadrilateral and triangle elements with bilinear and linear shape functions, respectively, are used for each computation.

2.5.1 Geometry 1

Geometry 1 is a square with a central hole as shown in Figure 2.2a. The domain of interest ω is an annulus around the hole. The square has side length 2, the hole radius 0.3, and ω radius 0.7. The parameter a=4, and b=1. The shear modulus $c(x) = 1000$ in the inclusions and $c(x) = 1$ in the matrix. The ensemble average

boundary displacement $\bar{g}(x) = \pm 0.1$, positive along the edges marked with dotted circles in Figure 2.2b and negative along edges marked with crossed circles, and $\bar{g}(x) = 0$ along the interior boundary $\partial\omega_I^*$ in Figure 2.2b. In Figure 2.6 the worst case energy concentration and the associated strain and stress fields are compared to the average ensemble load solution and the associated strain and stress fields.

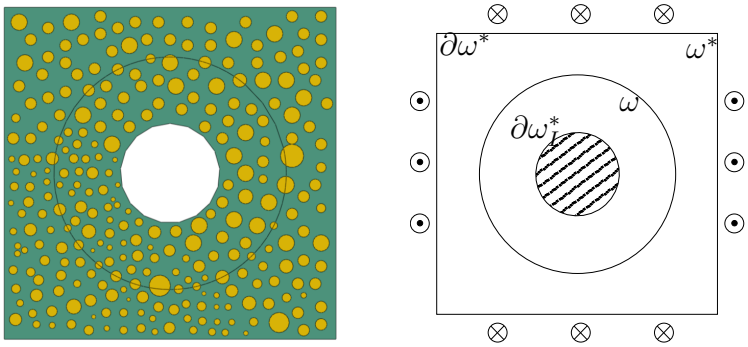

(a) (b)

FIGURE 2.2: Geometry 1. (a) The cross sectional layout. (b) The ensemble averaged Dirichlet boundary conditions for random loading. Crosses represent displacement into the page, dots out of the page.

2.5.2 Geometry 2

Geometry 2 is a rectangle with hole to one end as shown in Figure 2.3a. The domain of interest ω is an annulus around the hole. The rectangle has height 6 and width 2, the hole radius 0.5, and ω radius 0.85. The parameter a=8, and b=1. The shear modulus $c(x) = 1000$ in the inclusions and $c(x) = 1$ in the matrix. The ensemble average boundary displacement $\bar{g}(x) = \pm 0.1$ or 0 as shown in Figure 2.3b. Here diagonal lines along edges indicate portions of the outer boundary where $u = 0$. The computed fields are displayed in Figure 2.7.

2.5.3 Geometry 3

Geometry 3 is a cross with holes at all four ends as shown in Figure 2.4a. The domain of interest ω is an annulus around the top hole. The cross has a central square of side length 6 and arms of length 7 and width 6, the holes have radius 1.5,

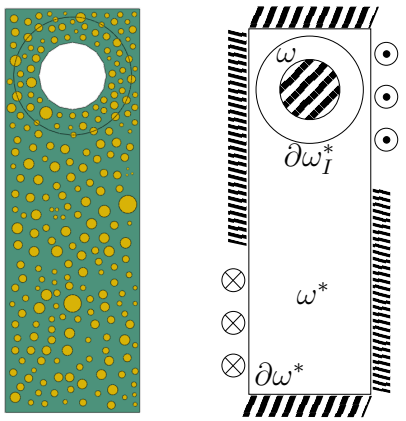

(a) (b)

FIGURE 2.3: Geometry 2. (a) The cross sectional layout. (b) The ensemble averaged Dirichlet boundary conditions. Crosses represent displacement into the page, dots out of the page.

and ω radius 2.5. The parameter a=40, and b=1. The shear modulus $c(x) = 1000$ in the inclusions and $c(x) = 1$ in the matrix. The ensemble average boundary displacement $\bar{g}(x) = \pm 0.1$ or 0 as shown in Figure 2.4b. The computed fields are displayed in Figure 2.8.

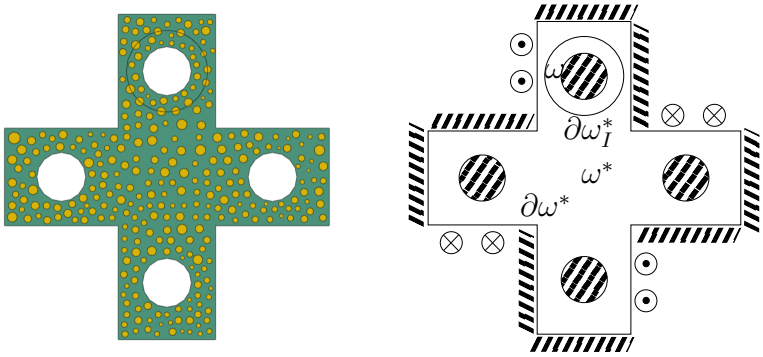

(a) (b)

FIGURE 2.4: Geometry 3. (a) The cross sectional layout. (b) The ensemble averaged Dirichlet boundary conditions. Crosses represent displacement into the page, dots out of the page.

2.5.4 Geometry 4

Geometry 4 is an L shaped bracket with hole at the top leg as shown in Figure 2.5a. The domain of interest ω is an annulus around the hole. The bracket has long edges

of length 6, short edges of length 4, and legs of width 2, the hole has radius 0.35, and ω radius 0.85. The parameter a=12, and b=1. The shear modulus $c(x) = 1000$ in the inclusions and $c(x) = 1$ in the matrix. The ensemble average boundary displacement $\bar{g}(x) = \pm 0.1$ or 0 as shown in Figure 2.5b. The computed fields are displayed in Figure 2.9.

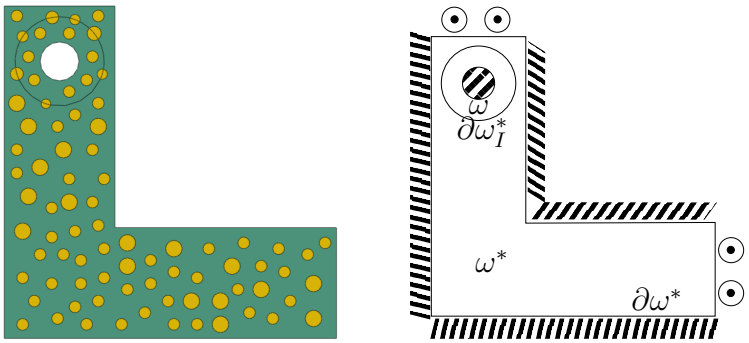

(a) (b)

FIGURE 2.5: Geometry 4. (a) The cross sectional layout. (b) The ensemble averaged Dirichlet boundary conditions. Crosses represent displacement into the page, dots out of the page.

TABLE 2.1: Computations of energy concentration for each geometry. The final column shows the number of functions used from the closed form KKL expansion given by (2.47)

Geometry	V	$\bar{P}_N$	$\hat{g}_n$, $\hat{g}'_n$
1	0.604	0.136	20, 17
2	0.695	0.149	36, 25
3	0.576	0.029	65, 63
4	0.686	0.072	54, 31

2.5.5 Observations

Figures 2.7a, 2.8a, and 2.9a show, as expected, that the worst case load concentrates energy around the portion of the boundary near the domain of interest. The overall shape of the concentration for the worst case load is influenced by the placement of the heterogeneities.

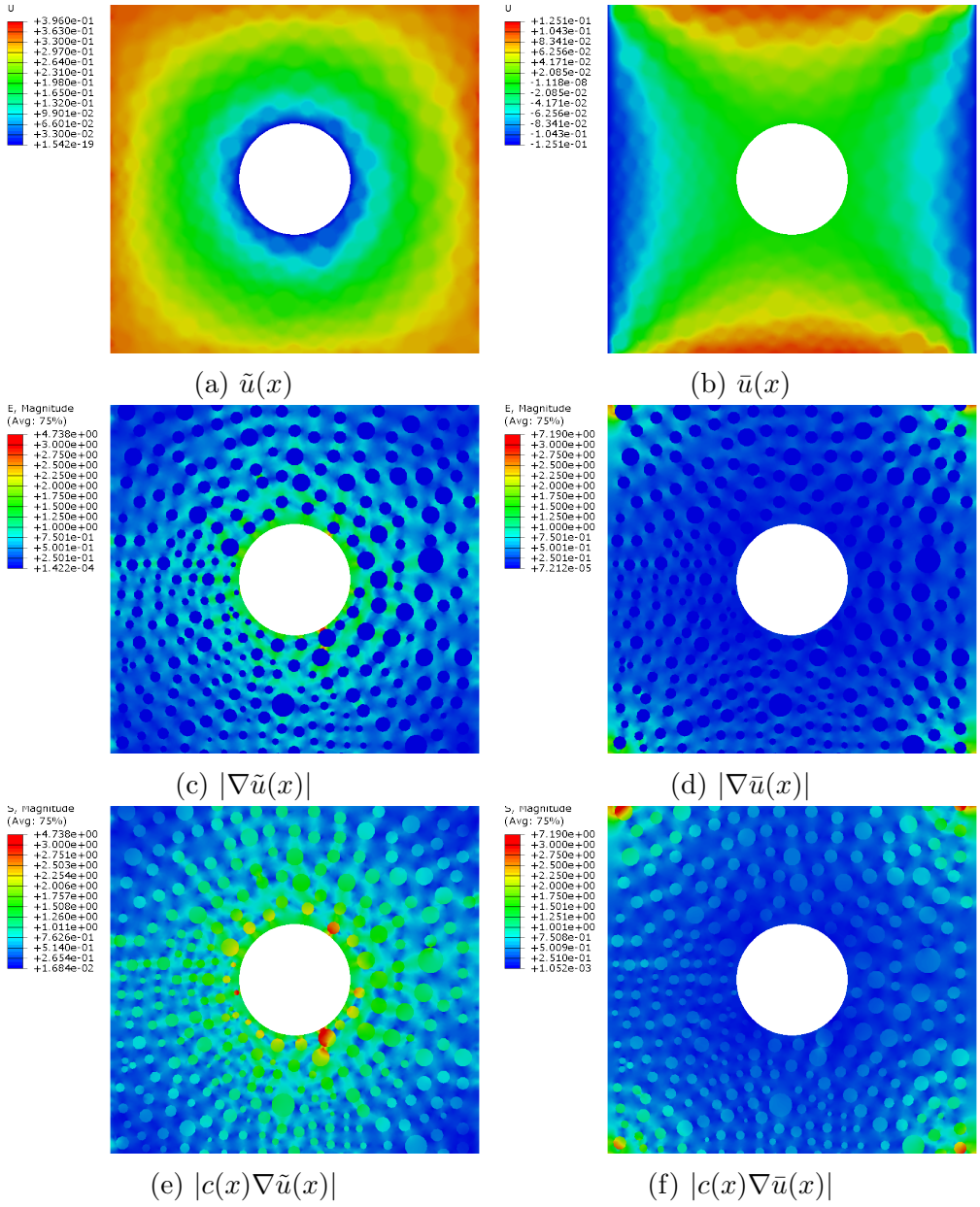

(a) $\tilde{u}(x)$ (b) $\bar{u}(x)$

(c) $|\nabla\tilde{u}(x)|$ (d) $|\nabla\bar{u}(x)|$

(e) $|c(x)\nabla\tilde{u}(x)|$ (f) $|c(x)\nabla\bar{u}(x)|$

FIGURE 2.6: Cross-section of Geometry 1. The worst case solution (a) $\tilde{u}$ and the corresponding (c) strain and (e) stress compared to the ensemble averaged solution (b) $\bar{u}$ and the corresponding (d) strain and (f) stress.

The expected energy concentration $\bar{P}_N$ is seen to be well below the worst case energy concentration V, as seen in Table 2.1. This large deviation is expected since the Markovian covariance leads to periodic boundary fluctuations (2.47) which distribute the random loads equally along the boundary. A less well-behaved covariance could close this gap somewhat; however, the expected energy concentration

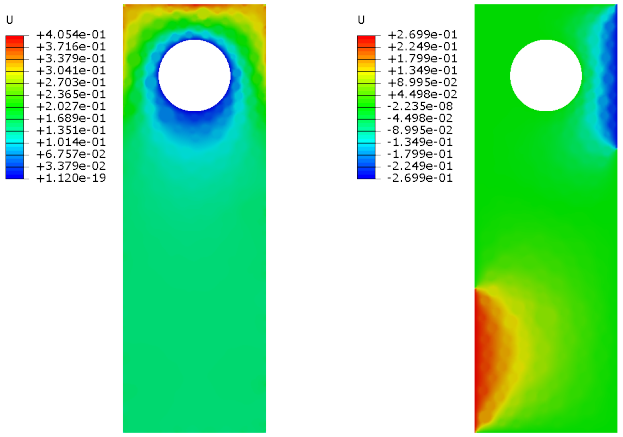

(a) $\tilde{u}(x)$

(b) $\bar{u}(x)$

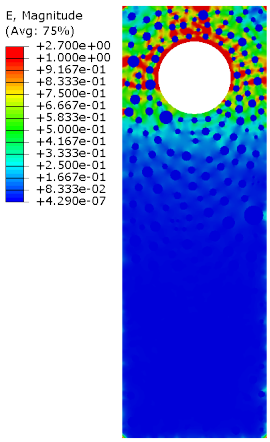

(c) $|\nabla\tilde{u}(x)|$

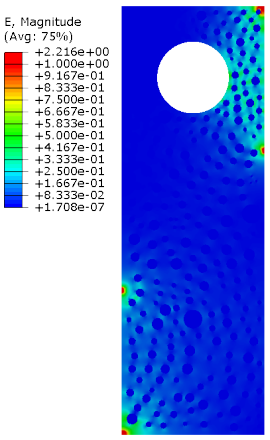

(d) $|\nabla\bar{u}(x)|$

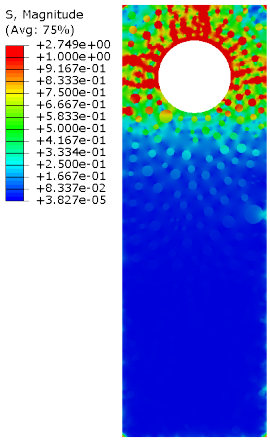

(e) $|c(x)\nabla\tilde{u}(x)|$

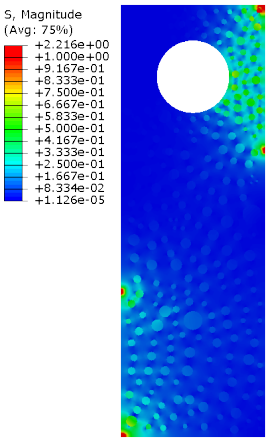

(f) $|c(x)\nabla\bar{u}(x)|$

FIGURE 2.7: Cross-section of Geometry 2. The worst case solution (a) $\tilde{u}$ and the corresponding (c) strain and (e) stress compared to the ensemble averaged solution (b) $\bar{u}$ and the corresponding (d) strain and (f) stress.

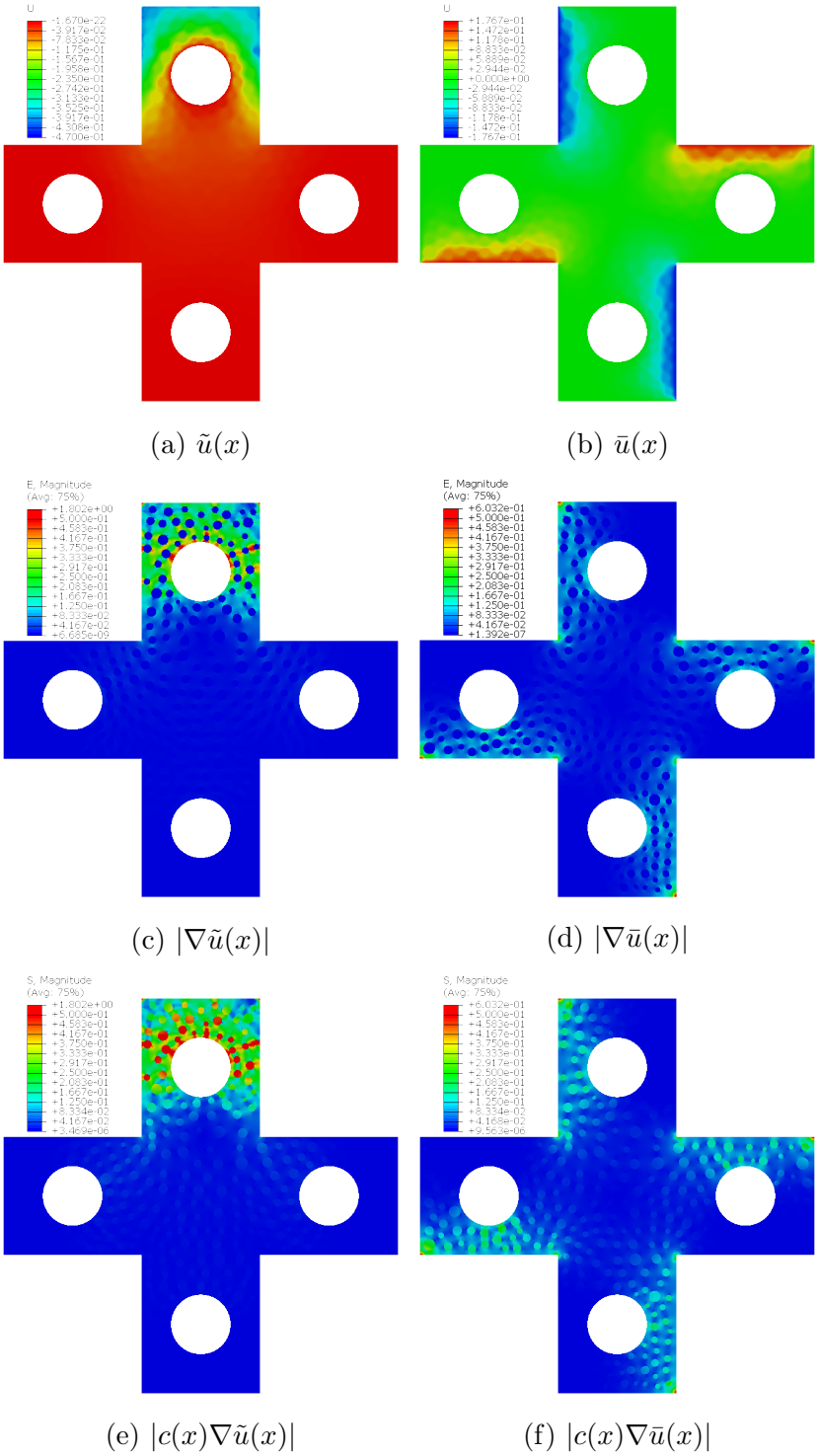

(a) $\tilde{u}(x)$ (b) $\bar{u}(x)$

(c) $|\nabla\tilde{u}(x)|$ (d) $|\nabla\bar{u}(x)|$

(e) $|c(x)\nabla\tilde{u}(x)|$ (f) $|c(x)\nabla\bar{u}(x)|$

FIGURE 2.8: Cross-section of Geometry 3. The worst case solution (a) $\tilde{u}$ and the corresponding (c) strain and (e) stress compared to the ensemble averaged solution (b) $\bar{u}$ and the corresponding (d) strain and (f) stress.

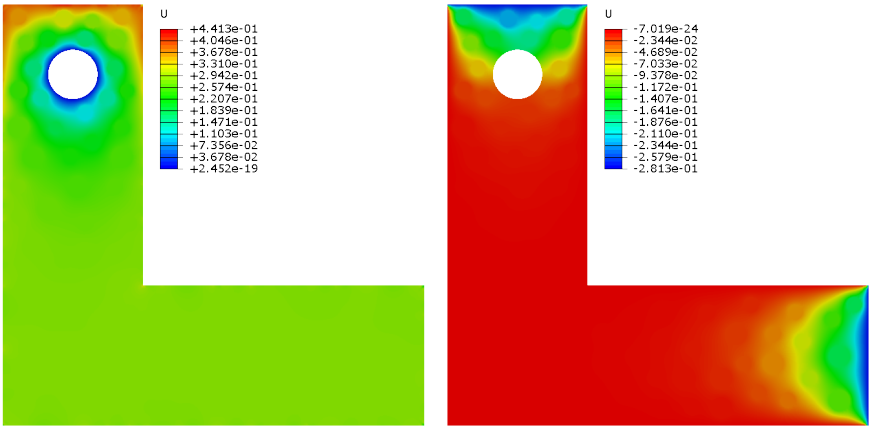

(a) $\tilde{u}(x)$

(b) $\bar{u}(x)$

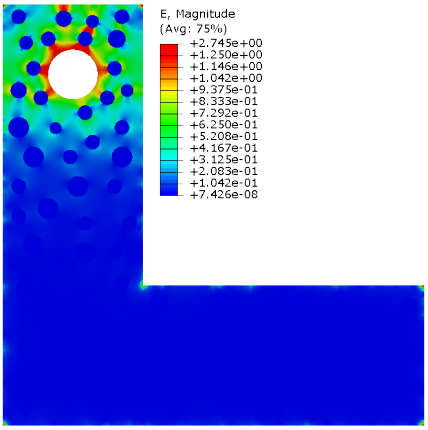

(c) $|\nabla\tilde{u}(x)|$

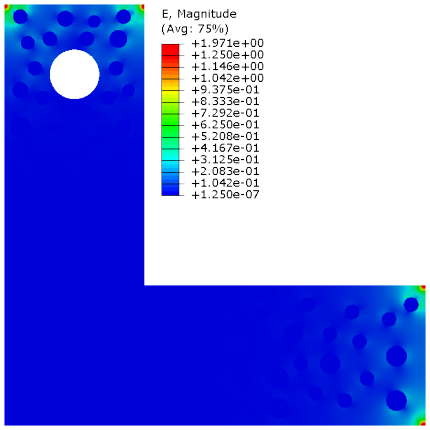

(d) $|\nabla\bar{u}(x)|$

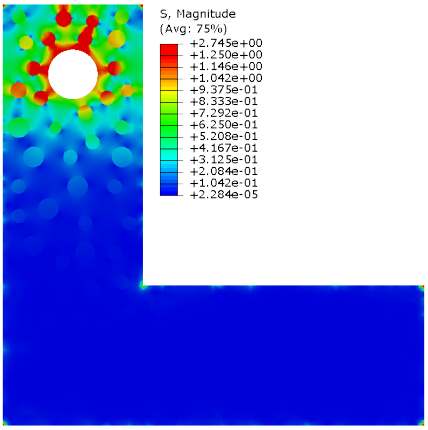

(e) $|c(x)\nabla\tilde{u}(x)|$

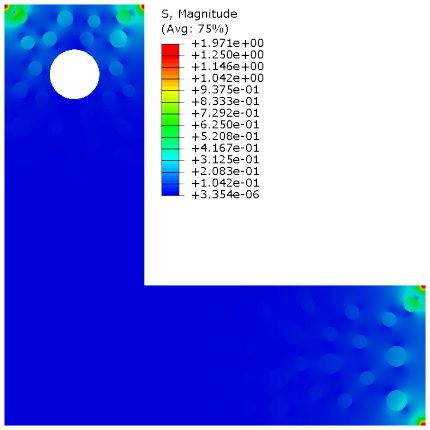

(f) $|c(x)\nabla\bar{u}(x)|$

FIGURE 2.9: Cross-section of Geometry 4. The worst case solution (a) $\tilde{u}$ and the corresponding (c) strain and (e) stress compared to the ensemble averaged solution (b) $\bar{u}$ and the corresponding (d) strain and (f) stress.

falls considerably below the largest possible energy concentration associated with a particular ensemble of loads.

2.6 Conclusions

We present a novel method for computing the worst case boundary load that imparts the maximum possible fraction of total energy onto a prescribed domain of interest contained within a composite structure. The method works for both Neumann or Dirichlet boundary conditions. The solution of the maximal energy concentration problem is given by an eigenvalue eigenfunction pair for the concentration eigenvalue problem. To illustrate the ideas this method is applied to four distinct geometries in the context of anti-plane shear. The the worst case loads are compared with the expected energy concentration of a random ensemble of loadings specified by a Markovian covariance with closed form solution using a KKL expansion. The expected energy penetration of the random loadings for Markovian covariance were seen to be substantially less than the maximal energy concentration associated with the worst case load. The method presented here provides a novel way to recover a rigorous upper bound on how 'bad' a random ensemble of loadings could be. The methods developed here can be used in evaluating and identifying worst case random loads with large energy concentration.

Alternatively one can apply these methods to evaluate the ability of a composite geometry, such as a functionally graded composite, to prevent energy penetration to a particular interior subdomain. This approach can then be used as a design tool to find the design most resistant to the worst case load.

Chapter 3

Implementation of Multiscale-Spectral GFEM and Optimal Oversampling

3.1 Introduction

In chapter 2 the motivation for computing stress and strain fields within multiscale composite materials was given. In this chapter we investigate a particular method for the computation of these fields via the Generalized Finite Element Method (GFEM) introduced in [3] and expanded on in [2], [8], and [32]. The GFEM is a partition of unity method (PUM), which allows for many independent local computations over the entire domain to be performed and brought back together through a partition of unity. The local computations are performed on overlapping subdomains, or patches, ω_i, $i = 1, \ldots, N$, over which local approximation spaces V_{ω_i}, which carry local information, may be constructed.

A natural question to ask is what local basis functions should be used. One approach is to use optimal oversampling spaces which concentrate the greatest amount of energy in an expanded patch $\omega_i^* \supset \omega_i$ into the smaller patch ω_i. The problem of solving for these functions given a domain ω_i^* and subdomain ω_i was precisely the topic of chatper 2. Using the aforementioned local basis functions in the context of the GFEM leads to the Multiscale Spectral Generalized Finite Element Method (MS-GFEM) introduced in [6] for the conductivity problem and extended to elasticity in [5].

The core concepts of the GFEM are briefly outlined and the optimal local shape functions from chapter 2 are redefined in the context of this method. The MS-GFEM algorithm is outlined and an implementation of the method is presented along with an example problem computed by this code. A method for speeding up the computations of the local basis functions is proposed and a numerical study

illustrating the method is discussed. Finally, a recently proven theorem of Lipton showing that the convergence rate of these local basis functions is independent of contrast is presented and a numerical convergence study supporting the theorem is discussed.

3.2 Problem Formulation

In this section we will formulate the problem in the variational form and the finite dimensional form for use with a finite element method.

3.2.1 Variational Formulation of the Problem

To fix ideas we consider the scalar problem over a bounded domain, $\Omega \subset \mathbb{R}^2$ with piecewise C^1-boundary, given by

$$-\operatorname{div}(A(x)\nabla u(x)) = f(x),\ x \in \Omega \tag{3.1}$$

with Neumann boundary conditions prescribed on the boundary $\partial\Omega_N \subset \partial\Omega$

$$n \cdot A(x)\nabla u(x) = g(x),\ x \in \partial\Omega_N, \tag{3.2}$$

where n is the unit outer normal vector, and Dirichlet boundary conditions on $\partial\Omega_D \subset \partial\Omega$

$$u(x) = h(x),\ x \in \partial\Omega_D, \tag{3.3}$$

such that $\partial\Omega_D \cap \partial\Omega_N = \emptyset$ and $\partial\Omega_D \cup \partial\Omega_N = \partial\Omega$. Here $A(x)$ is the 2×2 conductivity matrix with measurable coefficients $a_{ij}(x) \in L^\infty(\Omega)$, and satisfies ellipticity and boundedness conditions

$$0 \leq \alpha v \cdot v \leq A(x)v \cdot v \leq \beta v \cdot v < \infty,\ \forall x \in \Omega \text{ and } v \in \mathbb{R}^2 \tag{3.4}$$

We assume that the consistency condition is satisfied,

$$\int_{\partial\Omega_N} g\,dx + \int_{\Omega} f\,dx = 0. \tag{3.5}$$

The weak solution $u \in H^1_D(\Omega) = \{u \in H^1(\Omega) : u = h \text{ on } \partial\Omega_D\}$ of (3.1) satisfies

$$B(u, v) = F(v) \tag{3.6}$$

for all $v \in H^1_{0D} = \{v \in H^1(\Omega) : v = 0 \text{ on } \partial\Omega_D\}$ where

$$B(u, v) = \int_\Omega A(x)\nabla u \cdot \nabla v \, dx \text{ and } F(v) = \int_\Omega fv \, dx + \int_{\partial\Omega_N} gv \, ds. \tag{3.7}$$

The energy norm is given by $\|u\|_{\mathcal{E}(\Omega)} = (B(u, u))^{1/2}$.

3.2.2 Finite Dimensional Problem

The solution to (3.6) is computed here using MS-GFEM. In this section we outline the key concepts of the method. To fix ideas, we consider a computational domain $\Omega \subset \mathbb{R}^2$ containing smooth inclusions separated by a minimum distance. The GFEM is a domain decomposition given by a partition of unity of overlapping subdomains. Over each subdomain a local approximation space of shape functions is constructed. In the MS-GFEM the local shape functions are characterized by an optimal local approximation space obtained from oversampling. The local computations associated with construction of local approximation spaces are independent and can be performed in parallel. The resulting global stiffness matrix can be several orders of magnitude smaller than the stiffness matrix obtained by applying FEM directly ([6]).

We now describe the partition of unity. Let $\{\omega_i\}_{i=1}^m$ be a collection of open sets covering the domain Ω such that $\cup_{i=1}^N \omega_i = \Omega$ and let $\phi_i \in C^1(\omega_i)$, $i = 1, \ldots, m$, be a partition of unity subordinate to the open covering. The partition of unity

functions satisfy the following properties:

$$0 \leq \phi_i \leq 1, \quad i = 1, \ldots, N, \tag{3.8}$$

$$\phi_i(x) = 0,\ x \in \Omega \backslash \omega_i, \quad i = 1, \ldots, N, \tag{3.9}$$

$$\sum_i \phi_i(x) = 1 \quad \forall x \in \Omega, \tag{3.10}$$

$$\max_{x \in \Omega} |\phi_i(x)| \leq C_1, \quad i = 1, \ldots, N, \tag{3.11}$$

$$\max_{x \in \Omega} |\nabla \phi_i(x)| \leq \frac{C_2}{\operatorname{diam}(\omega_i)}, \quad i = 1, \ldots, N, \tag{3.12}$$

where C_1 and C_2 are bounded positive constants and $\operatorname{diam}(\omega_i)$ is the diameter of the set ω_i. The partition of unity functions are chosen to be flat-topped so that local approximation spaces are linearly independent and for ensuring good conditioning of the global stiffness matrix ([16]).

Let $\{\omega_i^*\}_{i=1}^N$ be a second covering such that each ω_i is compactly contained within the larger open set ω_i^*. For ω_i touching the boundary of Ω we write $\omega_i^* = \omega_i^* \cap \Omega$. In what follows we will refer to the subdomains ω_i and ω_i^* as patches.

The local approximations are separated into local particular solutions and a local approximation space $V_{\omega_i^*}^{m_i}$. Here the dimension of the local space is denoted by m_i. On each subdomain ω_i the local approximation space is created by constructing a finite dimensional space of functions on ω_i^* and restricting them to ω_i. The local shape functions describing a basis for $V_{\omega_i^*}^{m_i}$ are eigenfunctions associated with the singular values of the restriction operator (see section 3.2.3). The local functions are A-harmonic, i.e., they satisfy

$$-\operatorname{div}(A(x)\nabla \xi(x)) = 0 \text{ on } \omega_i^*. \tag{3.13}$$

The space of A-harmonic functions is written $H_A(\omega_i^*)$. These functions are chosen such that they are equivalent up to a constant. The associated quotient space is written $H_A(\omega_i^*)/\mathbb{R}$. If $\partial\omega_i \cap \partial\Omega \neq \emptyset$, the local functions are further restricted

such that they satisfy homogeneous Dirichlet boundary conditions on $\partial\omega_i^* \cap \partial\Omega_D$ and homogeneous Neumann conditions on $\partial\omega_i^* \cap \partial\Omega_N$. For interior subdomains and boundary subdomains with Neumann boundary conditions the local approximation space is augmented with the constant functions. In all cases the dimension of the local approximation space over ω_i is denoted by m_i. The global approximation space is constructed from the local approximation spaces and is defined by

$$V^N = \left\{ \sum_{i=1}^{N} \phi_i \xi_i : \xi_i \in V_{\omega_i^*}^{m_i} \right\}. \tag{3.14}$$

Local particular solutions $\chi_i \in H^1(\omega_i^*)$ are defined by

$$-\operatorname{div}(A(x)\nabla\chi_i(x)) = f(x),\ x \in \omega_i^*, \tag{3.15}$$

with Dirichlet data $\chi_i = 0$ on $\partial\omega_i^*$ for interior patches. For boundary patches, $\chi_i = 0$ on $\partial\omega_i^* \cap \Omega$ and χ_i satisfies the boundary data (3.2) and (3.3) on $\partial\omega_i^* \cap \partial\Omega$. The global particular solution u^F is defined as

$$u^F = \sum_{i=1}^{N} \phi_i \chi_i. \tag{3.16}$$

The finite dimensional approximate solution of (3.6) is posed over the convex space $K^N = V^N + u^F$. The problem becomes a variational inequality over the convex space K^N. Here we seek a solution $u^G \in V^N(\Omega)$ to the following problem for all $v \in V^N$

$$B(u^G, v) = F(v) - B(u^F, v). \tag{3.17}$$

The MS-GFEM approximate solution to (3.6) is given by $u_0 = u^G + u^F$. The existence of a unique solution $u_0 \in K^N$ follows from the standard theory of variational inequalities see, e.g., [12].

3.2.3 Optimal Local Approximation Spaces and MS-GFEM

The global space V^N is defined by pasting together optimal local subspaces defined over the subdomains $\omega_i \subset \Omega$, $1 \leq i \leq N$. This optimal local approximation space

was developed in [6] for the scalar problem (3.1), and extended to elasticity in [5]. We begin by restricting attention to a single subdomain ω and omit the subscript. The oversampling problem is defined over the larger subdomain $\omega^* \supset \omega$ and the local solution space is decomposed as

$$H^1(\omega^*) = H^0_A(\omega^*) \oplus H^1_0(\omega^*) \oplus \mathbb{R}, \tag{3.18}$$

where $H^0_A(\omega^*)$ is the space of zero-average A-harmonic functions defined as

$$H^0_A(\omega^*) = \{v \in H^1(\omega^*) : B(v,w) = 0 \text{ for all } w \in H^1_0(\omega^*) \text{ and } \int_{\omega^*} v\,dx = 0\}. \tag{3.19}$$

The spaces $H^0_A(\omega^*)$ and $H_A(\omega^*)/\mathbb{R}$ are isometric to each other and are orthogonal to $\mathbb{R}$ in $L^2(\omega^*)$. The spaces $H^0_A(\omega^*)$ and $H^1_0(\omega^*)$ are orthogonal with respect to the energy inner product $(\cdot,\cdot)_{\mathcal{E}(\omega^*)} = B(\cdot,\cdot)$. Elements u of $H^0_A(\omega^*)$ restricted to ω are approximated using an optimal local basis. The restriction operator P is defined by $Pu(x) = u(x)$ for x in ω. The restriction is a compact map from $H^0_A(\omega^*)$ into $H^0_A(\omega)$ and the optimal local basis on ω is given by the span of the eigenfunctions $\{\xi_j\}_{i=1}^{\infty}$ associated with the singular values $\{\lambda_j\}_{j=1}^{\infty}$ of the restriction operator

$$P^*P\xi_j = \lambda_j \xi_j, \tag{3.20}$$

see [6]. This space provides local shape functions and we see that MS-GFEM is a spectral approximation method. The optimality of this oversampling space is seen from the theory of Kolmogorov n-widths, [28]. How well an n-dimensional subspace $S(n) \subset H^0_A(\omega)$ approximates an oversampled function $u \in H^0_A(\omega^*)$ over ω is measured by the Kolmogorov n-width as

$$d_n(\omega,\omega^*) = \inf_{S(n)} \sup_{u \in H^0_A(\omega^*)} \inf_{v \in S(n)} \frac{\|Pu - v\|_{\mathcal{E}(\omega)}}{\|u\|_{\mathcal{E}(\omega^*)}}. \tag{3.21}$$

The optimal subspace achieving the infimum of (3.21) for $n = m$ is written as V^m_ω and is defined as the span of the first m eigenfunctions satisfying (3.20), see

[28]. These eigenfunctions can be computed explictly and are characterized in the following theorem.

Theorem 3.1 ([6], Theorem 3.2)**.** *The optimal approximation space is given by* $V_\omega^m = \text{span}\{\xi^1, \ldots, \xi^m\}$*, where* $\xi^j = P\phi^j$ *and* λ^j *and* ϕ^j *are the largest* m *eigenvalues and corresponding eigenfunctions that satisfy*

$$(\phi^j, \delta)_{\mathcal{E}(\omega)} = \lambda^j (\phi^j, \delta)_{\mathcal{E}(\omega^*)} \ \forall \delta \in H_A^0(\omega^*). \tag{3.22}$$

The functions $\{\phi^j\}_{j=1}^\infty$ *form a complete orthonormal set in* $H_A^0(\omega^*)$*.*

We introduce the positive constant L defined by

$$L = (Ke)^{(\gamma+1)/(1/d-\gamma)} \tag{3.23}$$

with

$$K = 2\frac{\gamma_d^{1/d}}{\sqrt{\pi}}(\frac{\beta}{\alpha})^{1/2}(\frac{1+\rho}{\rho}), \tag{3.24}$$

where α, β are defined as in (3.4) $d = 2, 3$ is the dimension of the domain $\Omega \subset \mathbb{R}^d$, γ_d is the volume of the unit d-ball, and ρ is the ratio of side lengths σ, σ^* of the square or cube patchs $\omega \subset \omega^*$, respectively, such that $(1+\rho)\sigma = \sigma^*$. Then for $0 < \gamma < 1/d$ we have the exponential decay given by

Theorem 3.2 (Theorem 3.3 or equation (3.27) of [6])**.** *For* $m > L$

$$d_m(\omega, \omega^*) = \sqrt{\lambda_{m+1}} \leq e^{-m^{\frac{\gamma}{1+\gamma}}}. \tag{3.25}$$

For $u_A \in H_A^0(\omega^*)$ *there exists* $\xi \in V_\omega^m$ *such that*

$$\|u_A - \xi\|_{\mathcal{E}(\omega)} \leq \lambda_{m+1} \|u_A\|_{\mathcal{E}(\omega^*)}. \tag{3.26}$$

With the above results and optimal local bases from oversampling on each of the subdomains $\{\omega_i\}_{i=1}^N$, the space V^N, constructed as in (3.14), has global error on Ω

controlled by local errors (Theorem 3.2) on the subdomains ω_i and has a bound on the decay of the relative error measured in the energy norm provided by the following theorem.

Theorem 3.3 ([6],Theorem 3.10)**.** *For all $m > L$, there exists $u^G \in V^N$ and a constant $\mathcal{K}$ independent of m such that the approximation $u_0 = u^G + u^F \in K^N$ satisfies*

$$\|u - u_0\|_{L^2(\Omega)} \leq \mathcal{K} e^{-m^{\left(\frac{\gamma}{1+\gamma}\right)}} \tag{3.27}$$

and

$$\|u - u_0\|_{\mathcal{E}(\Omega)} \leq \mathcal{K} e^{-m^{\left(\frac{\gamma}{1+\gamma}\right)}}. \tag{3.28}$$

It is evident that L depends on the contrast ratio β/α through K. We see that exponential decay holds rigorously for approximation spaces with dimensions larger than L. However L increases with the square root of the contrast ratio, i.e., $(\beta/\alpha)^{1/2}$. Thus the a priori estimates indicate that exponential decay occurs for approximation spaces of progressively larger dimension depending on contrast. On the other hand we can obtain contrast independent exponential convergence if we restrict the class of coefficients to matrix-inclusion composites. No assumption on the shape of the inclusions is made other than they have a differentiable boundary with Lipschitz continuous first derivative. Here "the matrix" refers to the connected phase that surrounds the included phase. It is assumed that there is a prescribed minimum distance δ separating the inclusions and that the boundary of any inclusion is at least distance δ from the boundary of ω^*. The coefficient is taken to be piecewise constant and given by

$$A(x) = \begin{cases} \alpha I, \text{ inside the inclusions,} \\ \beta I, \text{ inside the matrix.} \end{cases} \tag{3.29}$$

Our numerical experiments show an immediate exponential decay of the n-width functions for this class of coefficients, see section 3.4.5. The numerical experiments also show that the relative global approximation error is exponentially decaying independent of contrast, see sections 3.4, 3.6.

These numerical results are corroborated theoretically, in forthcoming work by Lipton, in which an exponential convergence independent of material contrast is demonstrated for inclusions having lower conductivity than the surrounding matrix material, i.e., $\alpha < \beta$. The result is stated here and will appear with proof in forthcoming work by Lipton, Sinz, and Stuebner.

Theorem 3.4 (Lipton 2017)**.**

$$d_m(\omega, \omega^*) \leq e^{-m^{\gamma/(\gamma+1)}}, \tag{3.30}$$

for $0 \leq \gamma < \frac{1}{d}$ *and* $m > \tilde{L} = 2\frac{\gamma_d^{1/d}}{\sqrt{\pi}} C^{-1/2} \frac{1+\rho}{\rho}$.

Here $\tilde{L}$ is independent of contrast and depends on the geometry of the oversampling domains ω and ω^*, as well as on the geometry of the composite explicitly through the constant C, which depends on the shape of the inclusions, the minimum distance δ separating inclusions from each other and from the boundary.With this we have the contrast independent convergence of the global GFEM approximations.

Theorem 3.5 (Lipton 2017)**.** *For matrix-inclusion composites with* $\alpha < \beta$ *and* $0 < \gamma < 1/d$ *one has for all* $N > \tilde{L}$*, a* $u^G \in V^N$ *and a constant* $\mathcal{K}$ *independent of* N *such that the approximation* $u_0 = u^G + u^F \in K^N$ *satisfies*

$$\|u - u_0\|_{L^2(\Omega)} \leq \mathcal{K} e^{-N^{\left(\frac{\gamma}{1+\gamma}\right)}} \tag{3.31}$$

and

$$\|u - u_0\|_{\mathcal{E}(\Omega)} \leq \mathcal{K} e^{-N^{\left(\frac{\gamma}{1+\gamma}\right)}}. \tag{3.32}$$

The eigenfunctions which are the optimal approximation functions, also called n-width functions, are computed for the particular geometry and microstructure Ω. They carry information about the local fields and allow for a reduction in the dimension of the global stiffness matrix by several orders of magnitude. The operation count is on the order of the number of inclusions in the domain Ω, see [5].

3.3 Computational Method

We now outline the implementation of MS-GFEM. We list the main steps in the algorithm and describe the construction of the global stiffness matrix, particular solutions, and right hand side of the global Galerkin scheme.

Recall that we wish to solve (3.6) using the optimal local bases pasted together over the computational domain $\Omega \subset \mathbb{R}^2$. Here we are given a matrix of material properties $A(x)$ together with Neumann and Dirichlet boundary conditions specified over the boundary of Ω. We begin by first creating a standard finite element mesh on the entire domain Ω, and the algorithm uses this mesh. Future implementations will use independent meshes over each patch ω_i enhancing the parallel nature of the local computations.

The steps in the MS-GFEM algorithm are as follows:

1. Define a covering of Ω by square patches $\{\omega_i\}_{i=1}^N$ and expand each patch $\{\omega_i^*\}_{i=1}^N$ such that $\omega_i \subset \omega_i^*$ are concentric and the ratio of side edges of ω_i to ω_i^* is greater than 0.

2. Construct partition of unity functions $\{\phi_i\}_{i=1}^N$ subordinate to $\{\omega_i\}_{i=1}^N$. In this work we use the standard linear and bilinear shape functions over triangles and squares to construct the partition of unity functions.

3. Solve local particular solutions $\{\chi_i\}_{i=1}^N$ satisfying (3.15). The boundary data on interior patches is given by $\chi_i = 0$ on $\partial\omega_i^*$. On boundary patches χ_i satisfies Neumann boundary data (3.2) or Dirichlet data (3.3) on $\partial\omega_i^* \cap \partial\Omega$ with $\chi_i = 0$ on $\partial\omega_i^* \cap \Omega$.

4. Construct right hand side of (3.17), denoted as r.

5. Construct finite dimensional local spaces, $S_{\omega_i^*}^{m_i} \subset H_A^0(\omega_i^*)$, using piecewise linear hat functions as boundary data.

6. Construct and solve the finite dimensional local spectral problems on ω_i^* to build the local spectral bases spanning the spaces $V_{\omega_i}^{m_i}$.

7. Construct the global stiffness matrix G in (3.17) with entries given by $B(u, v)$ for $u, v \in V^N$.

8. Solve the Galerkin formulation given by $\mathrm{G}\mathbf{x} = \mathbf{r}$.

9. The approximate solution to (3.17) is given by $u = u^G + u^F$.

We elaborate on the elements of this algorithm below and illustrate the computations for a simple partition of unity comprised of two subdomains in section 3.4. For computational generation of finite dimensional subspaces of $H_A^0(\omega_i^*)$ and the generation local spectral bases, see section 3.5.

3.3.1 Construction of Local Solution Spaces, $S_{\omega_i^*}^{m_i}$.

The material domain Ω is covered by square or hexahedral patches $\omega_1, \ldots, \omega_N$ with an expanded covering $\omega_1^*, \ldots, \omega_N^*$ such that $\omega_i \subset \omega_i^*$. We use the following notations. Let $\mathcal{H} = \{E_e\}_{e=1}^{n_{el}}$ be a finite element mesh of Ω, with elements E_e, which conforms to the boundaries of each patch ω_i and ω_i^*, $i = 1, \ldots, N$. The piecewise linear and bilinear shape functions are denoted $H_n(\alpha)$ where $\alpha = (\alpha_1, \alpha_2)$ are coordinates on

the reference element and $x = (x_1, x_2)$ are the Cartesian coordinates on the domain Ω. The map $\alpha_e : E_e \to \square$ is the change of coordinates map from the e-th element E_e to the reference element $\square$. An approximate solution space $S^{m_i}_{\omega_i^*} \subset H^0_A(\omega_i^*)$ is constructed from local FEM solutions of

$$\begin{cases} -\operatorname{div}(A(x)\nabla w_i^k(x)) = 0 \text{ for } x \in \omega_i^* \\ \qquad\qquad w_i^k(x) = h_i^k(x) \text{ for } x \in \partial\omega_i^*. \end{cases} \tag{3.33}$$

Here $h_i^k(x)$ is the k-th hat function defined by $h_i^k = 1$ at the k-th boundary node on $\partial\omega_i^* \cap \Omega$ and $h_i^k = 0$ at all other boundary nodes. For boundary patches, $\partial\omega_i^* \cap \partial\Omega \neq \emptyset$, only hat functions corresponding to interior nodes, $\partial\omega_i^* \cap \Omega$, are used as boundary data, and $h_i^k(x)$ satisfies homogeneous Neumann data on $\partial\omega_i^* \cap \partial\Omega_N$ and homogeneous Dirichlet data on $\partial\omega_i^* \cap \partial\Omega_D$. We write the k-th A-harmonic function over ω_i^* as

$$w_i^k(x) = \sum_{e=1}^{n_{el}} \sum_{l=1}^{n_{en}} \mathbf{w}_{i,e}^{k,l} H_l(\alpha_e(x)), \tag{3.34}$$

where $\mathbf{w}_{i,e}^k$ is the nodal displacement vector at the e-th element, $1 \leq e \leq n_{el}$, contained in ω_i^*, with $\mathbf{w}_{i,e}^{k,l}$ the component at the l-th node, $1 \leq l \leq n_{en}$.

3.3.2 Construction of Local Spectral Bases, $V^{m_i}_{\omega_i^*}$

Now we construct the space local approximation spaces $V^{m_i}_{\omega_i^*} = \operatorname{span}\{\xi_i^1, \ldots \xi_i^{m_i}\}$, where the ξ_i^j are the eigenfunctions corresponding to the m_i largest eigenvalues of

$$\mathrm{Q}_i \mathbf{x} = \lambda \mathrm{P}_i \mathbf{x}. \tag{3.35}$$

Here the entries of the matrices Q_i and P_i are given as

$$\mathrm{Q}_i^{jk} = (w_i^j, w_i^k)_{\mathcal{E}(\omega_i^*)} = \int_{\omega_i} A\nabla w_i^j \nabla w_i^k dx = \int_{\partial\omega_i} (n \cdot A\nabla w_i^j) w_i^k ds, \tag{3.36}$$

$$\mathrm{P}_i^{jk} = (w_i^j, w_i^k)_{\mathcal{E}(\omega_i)} = \int_{\omega_i^*} A\nabla w_i^j \nabla w_i^k dx = \int_{\partial\omega_i^*} (n \cdot A\nabla w_i^j) w_i^k ds, \tag{3.37}$$

where we have used $S^{m_i}_{\omega_i^*}$ as an approximate basis for $H^0_A(\omega_i^*)$ in the local spectral problems defined by (3.22). The k-th entry of the vector $\mathbf{x}$ in (3.35) is defined to be

the coefficient of the k-th basis function $w_i^k(x) \in S_{\omega_i^*}^{m_i}$. Thus, the q-th, $1 \leq q \leq m_i$, optimal shape function over ω_i^* is written as

$$\xi_i^q(x) = \sum_{k=1}^{m_i} \xi_i^{q,k} w_i^k(x), \tag{3.38}$$

with coefficients $\mathbf{x}_k = \xi_i^{q,k}$. Here the n-width functions are listed as $\{\xi_i^1, \xi_i^2, \ldots, \xi_i^{m_i}\}$, where the corresponding eigenvalues are listed in descending order $1 > \lambda_i^1 \geq \lambda_i^2 \geq \cdots \lambda_i^{m_i} > 0$ (P_i and Q_i are symmetric positive definite).

Combining (3.34) and (3.38) gives the n-width functions written in terms of the underlying finite element discretization

$$\xi_i^q(x) = \sum_{e=1}^{n_{el}} \sum_{k=1}^{m_i} \sum_{l=1}^{n_{en}} \xi_i^{q,k} \mathbf{w}_{i,e}^{k,l} H_l(\alpha_e(x)). \tag{3.39}$$

3.3.3 Global Stiffness Matrix and Right Hand Side

Using the bases for the local trial fields $V_{\omega_i^*}^{m_i}$, which are augmented by the constant functions for interior patches or patches with Neumann boundary conditions, the global trial field V^N is defined as in (3.14) by

$$V^N = \mathrm{span}\{\phi_i \xi_i^q : 1 \leq i \leq N,\ 1 \leq q \leq m_i,\ \text{and } \xi_i^q \in V_{\omega_i^*}^{m_i}\}. \tag{3.40}$$

For boundary patches on which Dirichlet boundary conditions are enforced, $\partial\omega_i \cap \partial\Omega_D \neq \emptyset$, the rigid body motions need not be added to $V_{\omega_i^*}^{m_i}$. The galerkin discretization defined by (3.17) gives the matrix equation $\mathrm{G}\mathbf{x} = \mathbf{r}$ where the stiffness matrix G is defined entrywise by

$$\mathrm{G}_{iqjr} = (\phi_i \xi_i^q, \phi_j \xi_j^r)_{\varepsilon(\Omega)}. \tag{3.41}$$

The ij-th block of G corresponds to cross products of functions from $\phi_i V_{\omega_i^*}^{m_i}$ and $\phi_j V_{\omega_j^*}^{m_j}$. The iq-th element of the unknown vector $\mathbf{x}$ is then the coefficient of the global trial function $\phi_i \xi_i^q$, so that we have the part of the solution corresponding

to the local A-harmonic contributions written

$$u^G = \sum_{i=1}^{N} \sum_{q=1}^{m_i} \mathbf{x}_i^q \phi_i \xi_i^q. \tag{3.42}$$

Likewise, the right hand side of (3.17) is written entrywise as

$$\mathbf{r}_{iq} = F(\phi_i \xi_i^q) - B(u^F, \phi_i \xi_i^q) = \int_\Omega f \phi_i \xi_i^q dx + \int_{\partial\Omega_N} g \phi_i \xi_i^q dS - \int_\Omega u^F \phi_i \xi_i^q dx. \tag{3.43}$$

With $\mathrm{G}\mathbf{x} = \mathbf{r}$ defined as above, solving for $\mathbf{x}$ gives the A-harmonic part of the solution (3.42). The approximate solution to (3.1) is given by

$$u_0 = u^G + u^F = \sum_{i=1}^{N} \sum_{q=1}^{m_i} \mathbf{x}_i^q \phi_i \xi_i^q + \sum_{i=1}^{N} \phi_i \chi_i. \tag{3.44}$$

3.4 Numerical Implementation for a Benchmark Problem

For the implementation of the MS-GFEM multiple partial differential equations have to be solved. Here any method to solve PDEs can be used. The finite element method is used in this implementation. Our problem domain has an underlying finite element mesh and overlapping patches are defined in terms of that mesh. In this implementation integration is done over the finite elements.

3.4.1 Problem Formulation

For demonstration of the numerical implementation we consider the following problem.

$$-\operatorname{div}(A \nabla u(x_1, x_2)) = 1, \ (x_1, x_2) \in \Omega \tag{3.45}$$

where Ω is a square $(-1, 1) \times (-1, 1)$. On the left and on the right there are Dirichlet boundary conditions applied

$$u(x_1, x_2) = 0, \ (x_1, x_2) \in \partial\Omega_D, \tag{3.46}$$

and the top and bottom are free

$$-n \cdot A \nabla u(x_1, x_2) = 0, \ (x_1, x_2) \in \partial\Omega_N. \tag{3.47}$$

The matrix A is given as

$$A = \begin{pmatrix} 100 & 0 \\ 0 & 100 \end{pmatrix}. \tag{3.48}$$

The problem was chosen because it has Neumann and Dirichlet boundary conditions and also a body force and the analytic solution is easily determined as

$$u(x_1, x_2) = \frac{1}{200}(1 - x_1^2). \tag{3.49}$$

The mesh consists of 6400 linear rectangular elements, 6561 nodes, and 2 patches are used.

3.4.2 Construction of Partition of Unity

We define a two patch covering $\{\omega_1, \omega_2\}$ of Ω by a square patch $\omega_1 = (-0.6, 0.6) \times (-0.6, 0.6)$ and a square annulus $\omega_2 = \Omega - ([-0.4, 0.4] \times [-0.4, 0.4])$. The expanded patches are defined as $\omega_1^* = (-0.8, 0.8) \times (-0.8, 0.8)$ and $\omega_2^* = \Omega - ([-0.2, 0.2] \times [-0.2, 0.2])$. The covering is shown in Figure 3.1.

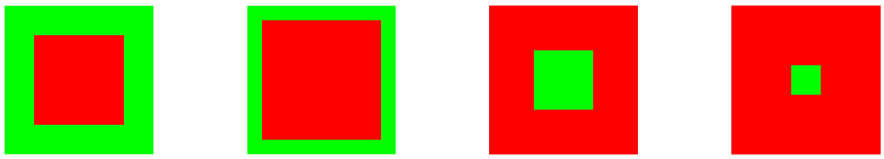

FIGURE 3.1: The patches ω_1, ω_1^*, ω_2, ω_2^* (left to right). Red indicates the subdomain, green is the area of Ω outside the subdomain.

To construct the partition of unity function ϕ_1 over ω_1, the overlap between ω_1 and ω_2 is determined and split into two sets as shown in Figure 3.2. In the middle square $(-0.2, 0.2) \times (-0.2, 0.2) \subset \omega_1$ the partition of unity function is 1, outside ω_1 it is 0. On the overlap shown on the left of Figure 3.2, ϕ_1 is linear. On the corners of the overlap, shown on the right, it is bilinear. The values of ϕ_1 are computed at the nodes and after that interpolated to the integration points using the finite

element shape functions. The partition of unity function ϕ_2 is then just $\phi_2 = 1 - \phi_1$. The partition of unity functions and their derivatives are shown in Figure 3.3.

FIGURE 3.2: Sets in the overlap of $\omega_1 \cap \omega_2$ shown in red. On the left region ϕ_1 is linear. On the right ϕ_1 is bilinear.

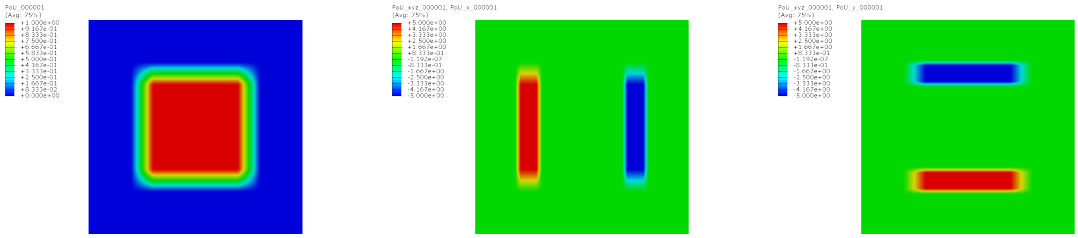

FIGURE 3.3: The partition of unity function ϕ_1 (left) and the derivatives with respect to x_1 (center) and x_2 (right) over Ω.

3.4.3 Local Particular Solutions

We find the local particular solutions χ_1 and χ_2 over ω_1^* and ω_2^*, respectively. On boundaries of the patches $\partial\omega_i^*$ which do not coincide with the outer boundary $\partial\Omega$ we enforce $\chi_i = 0$ and on boundaries which coincide with outer boundaries the given boundary conditions (3.46) and (3.47) are applied. For ω_1^* the problem becomes

$$\begin{cases} -\operatorname{div}(A\nabla\chi_1(x_1, x_2)) = 1, \ (x_1, x_2) \in \omega_1^* \\ \chi_1(x_1, x_2) = 0, \ (x_1, x_2) \in \partial\omega_1^*. \end{cases} \tag{3.50}$$

For ω_2^* the problem becomes

$$\begin{cases} -\operatorname{div}(A\nabla\chi_2(x_1,x_2)) = 1,\ (x_1,x_2) \in \omega_2^* \\ \chi_2(x_1,x_2) = 0,\ (x_1,x_2) \in \partial\omega_2^* \cap \Omega \\ \chi_2(x_1,x_2) = 0,\ (x_1,x_2) \in \partial\omega_2^* \cap \partial\Omega_D \\ -n \cdot A\nabla\chi_2(x_1,x_2) = 0,\ (x_1,x_2) \in \partial\omega_2^* \cap \partial\Omega_N. \end{cases} \tag{3.51}$$

The two particular solutions are shown in Figure 3.4. The two finite element analyses for χ_1 and χ_2, which includes the stiffness matrices and right hand sides, are saved so that their content is available for later computations.

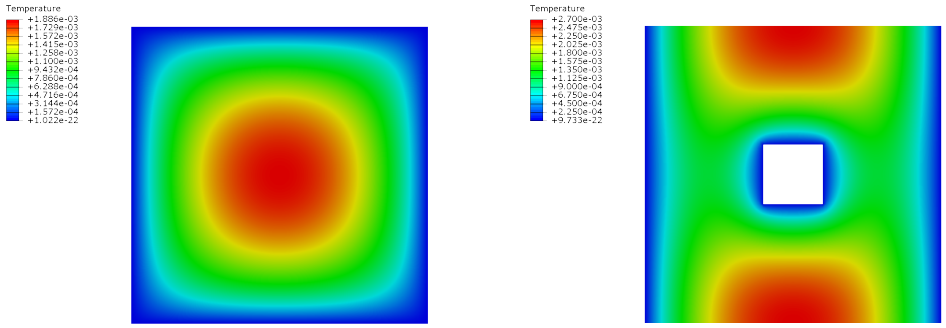

FIGURE 3.4: The particular solutions χ_1 (left) and χ_2 (right) displayed on ω_1^* and ω_2^*, respectively.

3.4.4 Construction of Local Solution Spaces, $S_{\omega_i^*}^{m_i}$

Next we construct local solution spaces $S_{\omega_i^*}^{m_i}$ using piecewise linear hat functions as boundary data. At each of the $1 \leq j \leq m_1$ nodes on $\partial\omega_1^*$ a uniform displacement is applied and the following problem is solved.

$$\begin{cases} -\operatorname{div}(A\nabla w_1^j(x,y)) = 0,\ (x,y) \in \omega_1^* \\ w_1^j(x,y) = 0.1, \text{ on the } j\text{-th node of } \partial\omega_1^* \\ w_1^j(x,y) = 0, \text{ everywhere else on } \partial\omega_1^*. \end{cases} \tag{3.52}$$

On ω_2^*, $S_{\omega_2^*}^{m_2}$ consists of functions corresponding to hat functions on $\partial\omega_2^* \cap \Omega$ as boundary data. Homogeneous Dirichlet and Neumann conditions are enforced on

$\partial\omega_2^* \cap \partial\Omega_D$ and $\partial\omega_2^* \cap \partial\Omega_N$, respectively. For each of the $1 \leq j \leq m_2$ nodes on $\partial\omega_2^* \cap \Omega$ the following problem is solved.

$$\begin{cases} -\operatorname{div}(A\nabla w_2^j(x,y)) = 0, \ (x,y) \in \omega_2^* \\ \qquad\qquad w_2^j(x,y) = 0.1, \text{ on the } j\text{-th node of } \partial\omega_2^* \cap \Omega \\ \qquad\qquad w_2^j(x,y) = 0, \text{ everywhere else on } \partial\omega_2^* \cap \Omega \\ \qquad\qquad w_2^j(x,y) = 0, \ (x,y) \in \partial\omega_2^* \cap \partial\Omega_D \\ -n \cdot A\nabla w_2^j(x,y) = 0, \ (x,y) \in \partial\omega_2^* \cap \partial\Omega_N. \end{cases} \tag{3.53}$$

Figure 3.5 shows two computed functions $w_i^j(x,y)$ over ω_1^* and ω_2^*. The figure

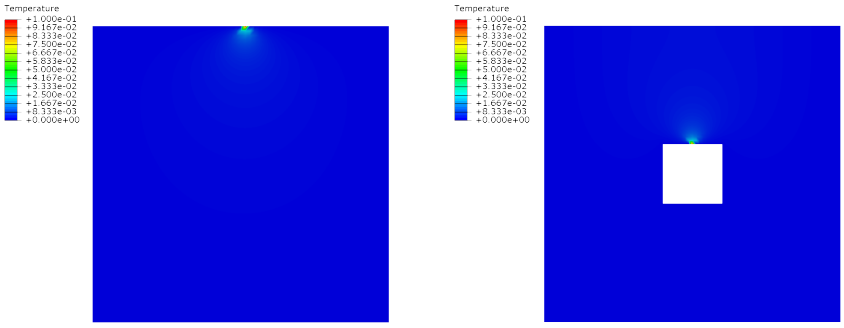

FIGURE 3.5: Two of the computed functions $w_1^j(x,y)$ (left) and $w_2^j(x,y)$ (right) shown over ω_1^* and ω_2^*, respectively, using a hat function with a single node as support for boundary data.

shows that the functions $w_i^j(x,y)$ are localized and decay rapidly away from the boundary when the hat function used as boundary data has support of only one node. A computation using a hat function with support over 11 nodes instead of one is shown in Figure 3.6. In section 3.5 we investigate using hat functions of different width supports to generate the local solution spaces, which reduces the number of problems to solve.

The stiffness matrices and right hand sides saved from the computations of (3.50) and (3.51) are used with modified boundary conditions. The systems are solved

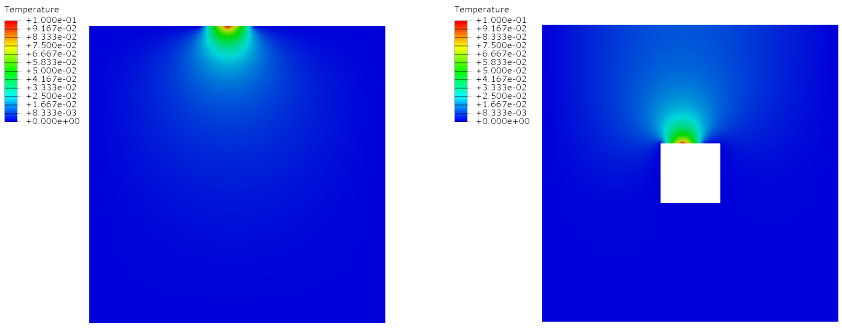

FIGURE 3.6: An example of A-harmonic functions w_i^j on ω_1^* (left) and ω_2^* (right) using a hat function with 11 nodes as support for boundary data.

directly. The functions w_i^j are saved at the nodes of the underlying finite element mesh and represented by finite element shape functions.

3.4.5 Construction of Local Spectral Bases

Now we construct the space $V_{\omega_i^*}^{m_i} = \{\xi_i^1, \ldots \xi_i^{m_i}\}$, where the ξ_i^j are the eigenfunctions corresponding to the m_i largest eigenvalues of

$$\mathrm{Q}_i\mathbf{x} = \lambda \mathrm{P}_i\mathbf{x} \tag{3.54}$$

with entries of P and Q defined as in (3.36) and (3.37). For this study the integration is performed over the domain rather than the boundary using the underlying finite elements, and, due to symmetry, only for the entries $j \geq k$. Equation (3.36) is written as

$$\int_{\omega_i} A\nabla w_i^j \nabla w_i^k \, dx = \sum_{e=1}^{N_{\omega_i}^e} (\mathbf{w}_{i,e}^j)^T \mathrm{K}_e \mathbf{w}_{i,e}^k, \tag{3.55}$$

where T denotes the transpose, $N_{\omega_i}^e$ is the number of elements in patch ω_i, $\mathbf{w}_{i,e}^j$ and $\mathbf{w}_{i,e}^k$ are the vectors of nodal values of the functions w_i^j and w_i^k at the element e, and K_e is the element stiffness matrix. The integral (3.37) over ω_i^* is computed by adding (3.55) to the integral over the set $\omega_i^* - \omega_i$. The summation is done in parallel using OpenMP. To ensure that the matrix P_i is positive definite, each row j of P_i and Q_i is normalized by P_i^{jj}.

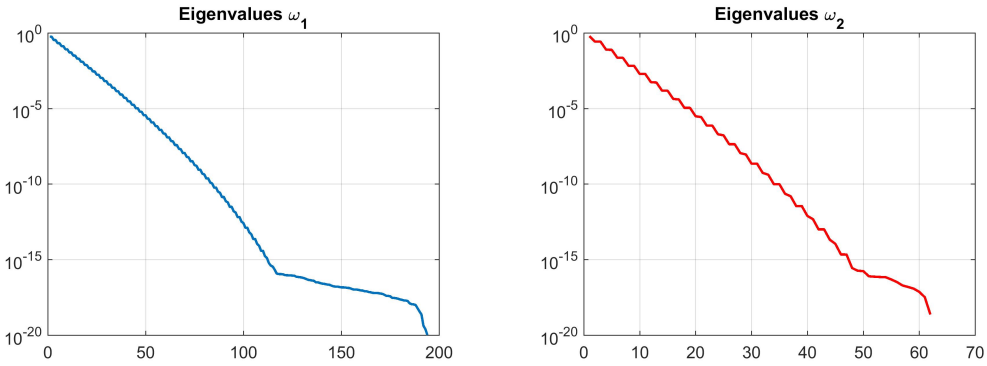

FIGURE 3.7: Log plot of eigenvalues for ω_1 (left) and ω_2 (right).

The generalized eigenvalue problems are then solved using routines from the Intel® Math Kernel Library (MKL). The problems are reduced to standard symmetric eigenvalue problems. In the following description of the methodology, we neglect the index i keeping in mind that the problem has to be solved for each patch. Considering that the matrix P is symmetric and positive definite, a Cholesky factorization is performed

$$\mathrm{P} = \mathrm{U}^T\mathrm{U} \tag{3.56}$$

where U is an upper triangular matrix. Equation (3.56) is then inserted in (3.54)

$$\mathrm{Q}\mathbf{x} = \lambda\mathrm{U}^T\mathrm{U}\mathbf{x}. \tag{3.57}$$

The inverse of U^T is computed and multiplied on both sides. On the left side there is also an identity matrix $\mathrm{I} = \mathrm{U}^{-1}\mathrm{U}$ inserted between Q and $\mathbf{x}$

$$\mathrm{U}^{T^{-1}}\mathrm{Q}\mathrm{U}^{-1}\mathrm{U}\mathbf{x} = \lambda\mathrm{U}\mathbf{x}. \tag{3.58}$$

With $\mathbf{y} = \mathrm{U}\mathbf{x}$ and $\mathrm{C} = \mathrm{U}^{T^{-1}}\mathrm{Q}\mathrm{U}^{-1}$ (3.58) becomes a standard eigenvalue problem

$$\mathrm{C}\mathbf{y} = \lambda\mathbf{y}. \tag{3.59}$$

The eigenvalues for problem (3.59) are the same as for (3.54), the eigenvectors $\mathbf{x}$ are obtained by solving $\mathrm{U}\mathbf{x} = \mathbf{y}$.

The eigenvalues for the two patches are shown in Figure 3.7. Eigenfunctions corresponding to eigenvalues which are smaller than 10^{-16} are discarded. One can see in the graph on the right that the eigenvalues come in pairs, due to symmetry, except for the first one of ω_2. Figure 3.8 shows ξ_1^4, ξ_1^8, ξ_2^1, and ξ_2^6. In addition to the local spectral basis functions, $V_{\omega_1^*}^{m_1}$ is augmented by the constant functions.

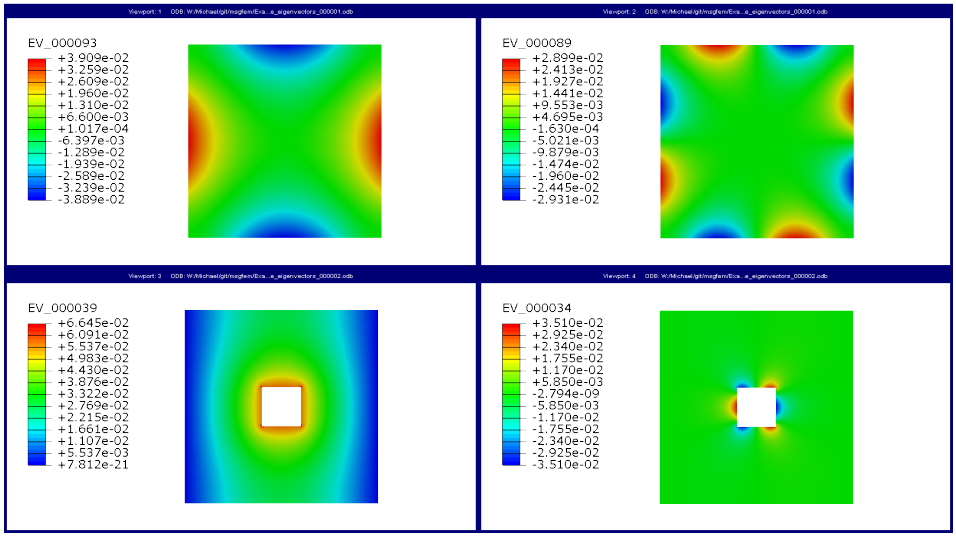

FIGURE 3.8: Local spectral basis functions ξ_1^4 (top left) and ξ_1^8 (top right) over ω_1^* and ξ_2^1 (bottom left) and ξ_2^6 (bottom right) over ω_2^*.

3.4.6 Solving the Global System, $\mathrm{G}\mathbf{x} = \mathbf{r}$

The global stiffness matrix and right hand side entries, (3.41) and (3.43), are computed using integration on the underlying finite element mesh similarly to (3.55) using the saved element stiffness matrices from the particular solution runs. The constructions of the global stiffness matrix and right hand side are performed in parallel using OpenMP.

The global system $\mathrm{G}\mathbf{x} = \mathbf{r}$ is solved using the Pardiso solver from the Intel® MKL. The solution vector $\mathbf{x}$ is used to recover u^G as in (3.42). The solution u^G is shown in Figure 3.9 (left). The particular solution u^F over the whole domain Ω consisting of the particular solutions over the patches glued together with the partition of unity functions is shown in Figure 3.9 (right).

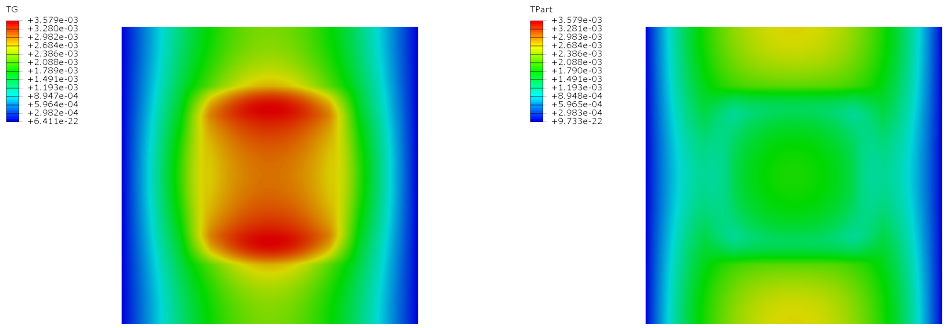

FIGURE 3.9: The solutions u^G (left) and u^F (right).

The final solution is then recovered from $u_0 = u^G + u^F$ shown in Figure 3.10 (left). The solution provided directly by a finite element method is displayed in Figure 3.10 (right) for comparison with the MS-GFEM solution. The MS-GFEM

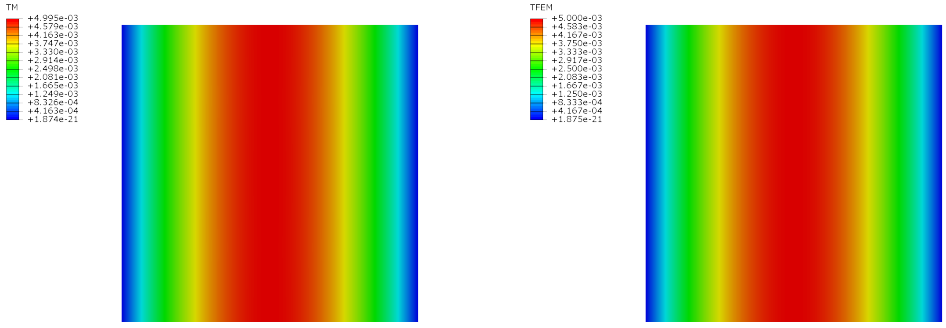

FIGURE 3.10: The final solution u_0 computed by the MS-GFEM (left) and an FEM (right).

computed solution has energy $\|u_0\|^2_{\mathcal{E}(\Omega)} = 0.0133077$. The analytic solution (3.49) has energy given by $\|u\|^2_{\mathcal{E}(\Omega)} = 0.0133333$. The relative error of the MS-GFEM solution compared to the analytic solution is given by

$$\frac{\|u - u_0\|_{\mathcal{E}(\Omega)}}{\|u\|_{\mathcal{E}(\Omega)}} = 4.2403318 \times 10^{-8}. \tag{3.60}$$

3.5 Computing Finite Dimensional Subspaces of $H_A(\omega_i^*)$ and Reduction of Computational Work

Generating the local solution spaces $S_{\omega_i^*}^{m_i} \subset H_A(\omega_i^*)$ can be computationally expensive for fine meshes. Defining the boundary data in (3.33) to use a single node for the support of the hat function h_i^j results in as many problems to solve as there are boundary nodes on $\partial\omega_i^*$. Additionally, we see from Figure 3.5 that the resulting function w_i^j has very small support. In Figure 3.6 A-harmonic functions with hat function boundary data having 11 nodes as support are shown, the functions w_i^j still have relatively small support. Each of these local problems (3.33) take approximately the same amount of time to solve. This motivates the usage of wider hat functions with more nodes for support. This results in fewer problems to solve, but also results in smaller spectral matrices in (3.35), since the number of A-harmonic functions w_i^j is equivalent to the number of hat functions used for boundary data. The number of local spectral basis functions ξ_i^j could therefore be reduced, however we see from Theorem 3.2 that the eigenvalues, which bound the local errors, decay at worst exponentially. For the example of section 3.4, the eigenvalues decay rapidly, seen in Figure 3.7, and numerical errors result past 100 and 50 for ω_1 and ω_2, respectively, so some eigenfunctions need to be discarded. We may therefore solve for fewer eigenfunctions and can use smaller P and Q matrices, meaning we do not need as many A-harmonic functions in the space $S_{\omega_i^*}^{m_i}$.

If the number of hat functions is reduced from N to M by defining the hat functions over larger supports then the computational time for constructing $S_{\omega_i^*}^{m_i}$ is reduced by a factor of $\frac{M}{N}$. The time for computing each entry of the matrices (3.36) and (3.37) is approximately the same. Because of symmetry of the matrices only the upper triangular part and the diagonal need to be computed. If N hat functions were used then $\frac{N(N+1)}{2}$ entries have to be computed. If that number is

reduced to M then

$$\frac{M(M+1)}{2} = \frac{N\rho\,(N\rho+1)}{2} \tag{3.61}$$

entries have to be computed, where $\rho = M/N$. For large values of N

$$\frac{M(M+1)}{2} \sim \frac{N^2\rho^2}{2}, \tag{3.62}$$

and the computational time for generating the matrices is reduced by a factor of $\left(\frac{M}{N}\right)^2$. The number of hat functions used for each successive widening progresses as $\{N, N/2, N/3, N/4, \ldots\}$. For example, if the support of the hat functions is increased from 1 to 3 nodes, then the total number of boundary value problems (3.33) to solve is $M = N/2$ and the time to fill the spectral matrices is about $1/4$ the time as with single node hat functions. We illustrate these observations with the following example.

We solve the problem

$$\begin{cases} -\operatorname{div}(A(x_1,x_2)\nabla u(x_1,x_2)) = 0,\ (x_1,x_2) \in \Omega \\ \qquad\qquad u(x_1,x_2) = 0,\ (x_1,x_2) \text{ on the left of } \partial\Omega \\ \qquad\qquad u(x_1,x_2) = 1,\ (x_1,x_2) \text{ on the right of } \partial\Omega \\ n \cdot A\nabla u(x_1,x_2) = 0,\ (x_1,x_2) \text{ on the top and bottom of } \partial\Omega. \end{cases} \tag{3.63}$$

on the domain shown in Figure 3.11 using hat functions with varying widths to generate the local solution spaces $S^{m_i}_{\omega_i^*}$. The domain Ω is a 20×10 rectangle with 100 circular inclusions. We label solutions $u_k,\ k = 1, 3, 5, 7, 9, \ldots,$ where k represents the number of nodes in the support of the hat function used as boundary data for problem (3.33). The matrix material has conductivity A_1 and the inclusion material has conductivity A_2. We compute solutions to (3.63) using two different sets of material properties. For Case 1

$$A_1 = \begin{pmatrix} 1 & 0 \\ 0 & 1 \end{pmatrix} \quad A_2 = \begin{pmatrix} 100 & 0 \\ 0 & 100 \end{pmatrix}, \tag{3.64}$$

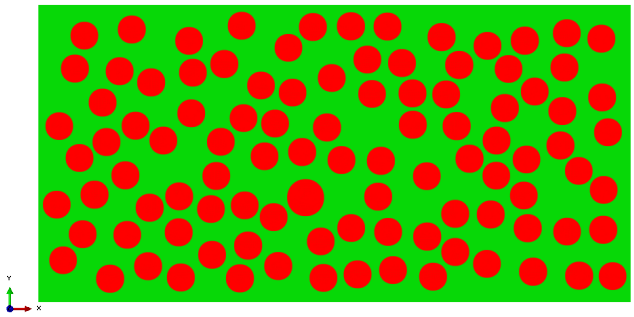

FIGURE 3.11: Rectangular domain of size 20×10 with 100 inclusions for problem (3.63).

and for Case 2 we reverse the material properties to

$$A_1 = \begin{pmatrix} 100 & 0 \\ 0 & 100 \end{pmatrix} \quad A_2 = \begin{pmatrix} 1 & 0 \\ 0 & 1 \end{pmatrix}. \tag{3.65}$$

The computations are done on a mesh with 201760 elements. The relative error of the final solutions u_k as compared to u_1 is computed with respect to the energy norm as

$$E_k = \frac{\|u_k - u_1\|^2_{\mathcal{E}(\Omega)}}{\|u_1\|^2_{\mathcal{E}(\Omega)}}. \tag{3.66}$$

The errors are reported in Table 3.1 and are graphed in Figure 3.12. The table also shows the execution time of the entire MS-GFEM algorithm for computing the solution u_k as well as the size of the spectral matrices and the number of eigenfunctions used in the computation of u_k. Figure 3.13 shows the relative errors of the relative eigenvalues with respect to the eigenvalues computed for u_1 as

$$E^j_{ki} = \frac{|\lambda^j_{1i} - \lambda^j_{ki}|}{|\lambda^1_{ki}|} \tag{3.67}$$

where E^j_{ki} is the relative error of the j-th eigenvalue of patch i corresponding to u_k with respect to the j-th eigenvalue corresponding to u_1.

In this example the eigenvalues show good agreement for the first three wider width hat functions (3, 7, and 9 nodes) in Figure 3.13, and it is for these wider hat

TABLE 3.1: Relative error for solutions using hat functions with different numbers of boundary nodes for support. The first column indicates the number of nodes in the support of the hat functions. The error is measured in the energy norm for Case 1 in which the matrix material has conductivity 1 and the inclusions 100, and Case 2 the reverse conductivities. Execution time for entire MS-GFEM run using different width hat functions. Also the size of the spectral matrices (number of hat functions used), and the number of local spectral basis functions used in the approximation.

				Eigenvalue System Size		Number of Eigenfunctions	
#	Error 1	Error 2	Time (s)	ω_1	ω_2	ω_1	ω_2
1	0	0	9668	1373	343	121	49
3	9.86E-08	6.04E-09	3323	686	172	122	49
5	8.35E-08	4.86E-09	1969	457	115	122	49
7	1.41E-07	4.64E-09	1466	343	86	122	48
9	8.22E-08	1.12E-08	1187	272	69	121	50
11	8.88E-08	8.18E-09	1046	228	58	119	46
13	1.54E-07	1.30E-08	905	196	49	116	45
15	1.90E-07	1.33E-08	826	171	43	116	42
17	1.79E-07	1.58E-08	747	152	39	108	38
19	1.96E-07	1.60E-08	685	137	35	101	35
21	2.14E-07	1.72E-08	628	124	32	93	32
23	2.56E-07	2.44E-08	589	114	29	88	29
25	2.98E-07	1.99E-08	553	105	27	83	27

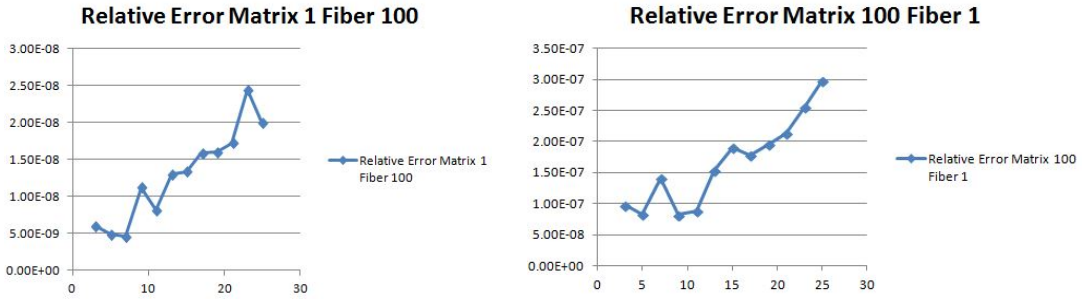

FIGURE 3.12: Plots of relative error versus the number of nodes in the support of the hat functions used for material properties defined by Case 1 and Case 2.

functions that the greatest reduction in execution time is observed in Figure 3.14. The agreement in the eigenvalues suggests that the local spectral bases are also in reasonable agreement. The number of eigenfunctions computed by the code remains

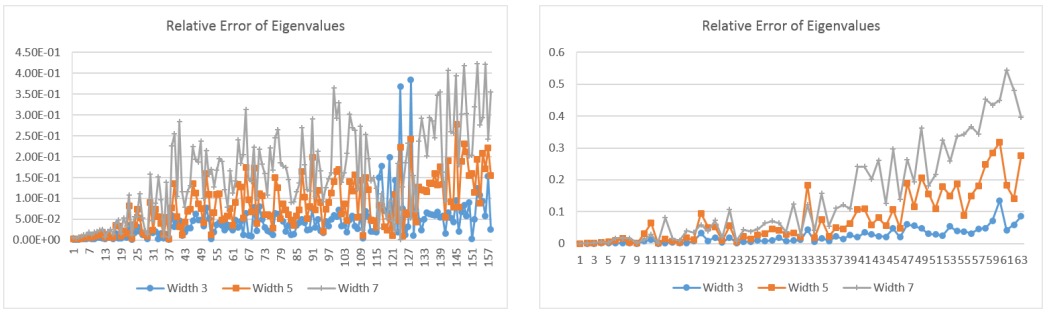

FIGURE 3.13: Plots of relative error of eigenvalues for hat functions of widths 3, 5, and 7 for Case 1 over ω_1 (left) and ω_2 (right).

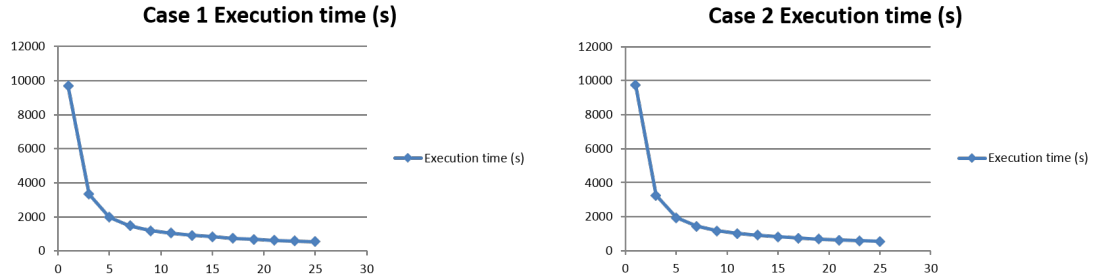

FIGURE 3.14: Plots of execution time of the MS-GFEM code against k, the width of hat functions used for Case 1 (left) and Case 2 (right).

the same for the first few wider hat functions. The relative error is observed to grow roughly linearly with respect to the widening of the hat functions in Figure 3.12. Collecting these observations, we conclude that this method of generating the local A-harmonic space $S^{m_i}_{\omega_i^*}$ is an effective method to reduce computational costs while maintaining acceptable error tolerance.

3.6 Contrast Independent Convergence Study

We discuss below numerical results indicating that the constant for the convergence rate in Theorem 3.4 is independent of contrast between material properties of the matrix material and the material of the separated circular inclusions.

3.6.1 High Conductivity Matrix with Low Conductivity Inclusions

To demonstrate the contrast independent convergence rate we consider again problem (3.63) but over a different domain Ω. In this example Ω is the 20×10 rectangular domain with 1000 circular inclusions shown in Figure 3.15. The matrix

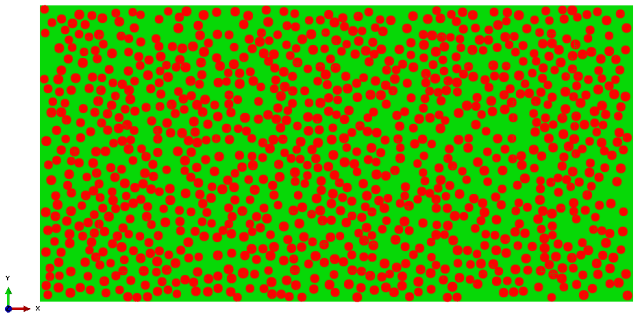

FIGURE 3.15: Problem (3.63) domain Ω with 1000 inclusions for convergence study.

material has property A_1 and the inclusion material has property A_2. They are given as

$$A_1 = \begin{pmatrix} \alpha & 0 \\ 0 & \alpha \end{pmatrix} \quad A_2 = \begin{pmatrix} 1 & 0 \\ 0 & 1 \end{pmatrix}, \tag{3.68}$$

where the constant α takes the values 2, 10, 100, 1,000, 10,000, 100,000, and 1,000,000 for each case in the study. The computations are carried out on a mesh with 74799 elements. The errors are computed relative to an overkill solution $u_0 = u_{76}^{30}$ which uses 76 local spectral shape functions for ω_1 and 30 for ω_2. The relative error with respect to the energy norm is computed as

$$E_i^j = \frac{\|u_0 - u_i^j\|^2_{\mathcal{E}(\Omega)}}{\|u_0\|^2_{\mathcal{E}(\Omega)}}, \tag{3.69}$$

where i and j are the number of local basis functions used from ω_1 and ω_2, respectively, used in computing the solution u_i^j of (3.63). We compute solutions u_i^j for $(i, j) = (5, 2)$ and increment i by 5 and j by 2 for each additional solution up to u_{70}^{28}. The decimal logarithm of the errors are shown in Table 3.2. A graph of the data is shown in Figure 3.16.

We observe that the error decays exponentially in Figure 3.16 up until $(35, 14)$ local basis functions are used, at which point the error levels out. This is likely due to the swift decay of the eigenvalues which bound the local errors, indicating

TABLE 3.2: Logarithm of the error for different contrasts for a high conductivity matrix and low conductivity inclusions computed on a mesh of 74799 elements.

ω_1	ω_2	$2:1$	$10:1$	$10^2:1$	$10^3:1$	$10^4:1$	$10^5:1$	$10^6:1$
5	2	-1.944	-1.834	-1.819	-1.817	-1.816	-1.816	-1.816
10	4	-3.035	-2.859	-2.897	-2.910	-2.912	-2.912	-2.912
15	6	-3.704	-3.400	-3.545	-3.581	-3.586	-3.586	-3.586
20	8	-4.166	-3.907	-4.071	-4.111	-4.116	-4.116	-4.116
25	10	-4.771	-4.511	-4.672	-4.709	-4.713	-4.714	-4.714
30	12	-5.318	-5.160	-5.194	-5.197	-5.198	-5.198	-5.198
35	14	-5.910	-5.597	-5.491	-5.472	-5.471	-5.471	-5.471
40	16	-5.943	-5.628	-5.531	-5.513	-5.513	-5.512	-5.512
45	18	-6.001	-5.687	-5.576	-5.555	-5.554	-5.554	-5.554
50	20	-6.109	-5.754	-5.615	-5.591	-5.589	-5.589	-5.589
55	22	-6.142	-5.781	-5.646	-5.620	-5.619	-5.619	-5.619
60	24	-6.265	-5.842	-5.695	-5.668	-5.667	-5.667	-5.667
65	26	-6.482	-6.162	-6.039	-5.999	-5.997	-5.997	-5.997
70	28	-6.572	-6.529	-6.565	-6.471	-6.471	-6.471	-6.471

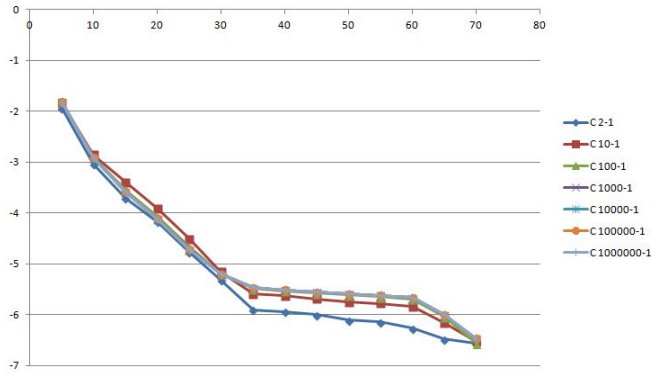

FIGURE 3.16: Log plot of error versus number of local basis functions used from ω_1. Each line is for a different contrast of material properties.

that the local basis functions past $(35, 14)$ make only a small contribution to the overkill solution u_0 and most of the local field information is carried by the first $(35, 14)$ local basis functions. The figure clearly indicates that the convergence rate is independent of material contrast.

3.6.2 Low Conductivity Matrix with High Conductivity Fibers

Here we again solve problem (3.63) over the domain shown in Figure 3.11 with 100 inclusions. The matrix material has property A_1 and the inclusion material has

property A_2 given as

$$A_1 = \begin{pmatrix} 1 & 0 \\ 0 & 1 \end{pmatrix} \quad A_2 = \begin{pmatrix} \beta & 0 \\ 0 & \beta \end{pmatrix}, \tag{3.70}$$

where the constant β takes the values 2, 5, 10, 20, 50, 100, 200, and 500. The computations are done on a mesh with 201760 elements. An overkill solution u_0 uses 101 shape functions from ω_1 and 40 from ω_2. Solutions u_i^j are computed for $(i, j) = (5, 2)$ with i incrementing in steps of 5 and j in steps of 2 ending at $(i, j) = (80, 32)$. The errors are computed using (3.69). The decimal logarithm is then taken. The graphs are shown in Figure 3.17. The convergence rates seem to be contrast dependent. That suggests to use a finer mesh to compute the gradients. In a second attempt a mesh with 588483 elements is used. The computations are repeated and the results are shown in Figure 3.18 and Table 3.3.

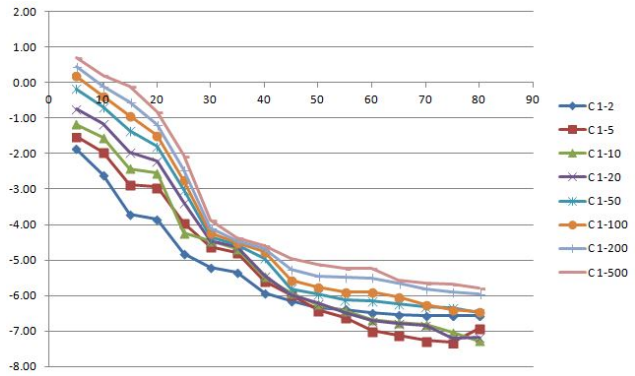

FIGURE 3.17: Logarithmic energy error for different contrasts.

The convergence rate ceases to be dependent on contrast once $(60, 24)$ local basis functions are used to compute the global solution. This supports Theorem 3.3 which states that the exponential bound and convergence rate only hold once the total number of local shape functions on all patches exceeds some constant L.

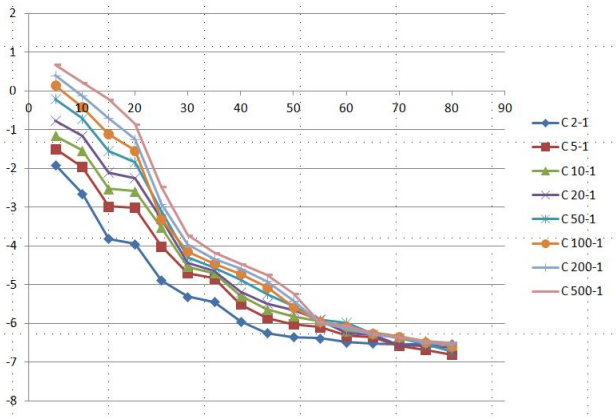

FIGURE 3.18: Logarithmic energy error for different contrasts.

TABLE 3.3: Logarithm of the error for different contrasts for a low conductivity matrix and high conductivity inclusions computed on a mesh of 588483 elements.

ω_1^*	ω_2^*	1 : 2	1 : 5	1 : 10	1 : 20	1 : 50	1 : 100	1 : 200	1 : 500
5	2	-1.900	-1.495	-1.152	-0.764	-0.205	0.150	0.403	0.682
10	4	-2.645	-1.956	-1.532	-1.155	-0.709	-0.405	-0.122	0.221
15	6	-3.816	-2.974	-2.524	-2.100	-1.538	-1.112	-0.701	-0.211
20	8	-3.942	-3.004	-2.582	-2.242	-1.833	-1.534	-1.241	-0.855
25	10	-4.888	-4.006	-3.524	-3.292	-3.105	-3.310	-2.911	-2.467
30	12	-5.306	-4.702	-4.531	-4.428	-4.287	-4.144	-3.969	-3.717
35	14	-5.438	-4.837	-4.700	-4.643	-4.553	-4.452	-4.332	-4.176
40	16	-5.945	-5.506	-5.291	-5.188	-4.873	-4.719	-4.587	-4.460
45	18	-6.245	-5.854	-5.642	-5.485	-5.236	-5.057	-4.902	-4.743
50	20	-6.351	-6.024	-5.811	-5.662	-5.541	-5.581	-5.415	-5.222
55	22	-6.378	-6.095	-5.933	-5.894	-5.907	-5.963	-5.992	-5.955
60	24	-6.485	-6.322	-6.208	-6.250	-5.976	-6.068	-6.137	-6.060
65	26	-6.513	-6.348	-6.234	-6.299	-6.277	-6.264	-6.283	-6.255
70	28	-6.545	-6.576	-6.340	-6.562	-6.385	-6.340	-6.364	-6.361
75	30	-6.535	-6.680	-6.449	-6.587	-6.547	-6.488	-6.500	-6.466
80	32	-6.539	-6.801	-6.567	-6.620	-6.730	-6.584	-6.543	-6.498
85	34	-6.679	-6.490	-7.096	-6.465	-6.701	-6.587	-6.496	-6.439
90	36	-7.043	-6.650	-7.210	-6.742	-6.824	-6.644	-6.758	-6.684

3.7 Conclusions

We have presented a numerical results showing that the local spectral basis functions developed in [6] and [5] have a convergence rate independent of material contrast for the conductivity problem with isolated inclusions having lower con-

ductivity than the surrounding matrix material. These results corroborate a recent theoretical result by Lipton, and further suggest that exponential convergence holds for the reverse contrast case as well. It was observed that the dependence on the underlying finite element mesh is more sensitive for the latter case.

The MS-GFEM numerical method was shown to be a viable method for the computation of local fields in heterogeneous materials of any contrast of material properties. A full implementation of the method along with the theoretical foundation of the method were discussed. A method for reducing computational costs in computing local trial fields was presented along with numerical results supporting the idea. In future work the implementation of MS-GFEM discussed here will be further parallelized for use on large scale computers. For much larger problems with many patches greater savings from computational costs are anticipated by using coarser hat functions. We finish by noting that in [30] similar work has been concurrently carried out showing contrast independence of the local spectral basis functions on their domains rather than of the global solutions, and the local spectral basis functions are shown to outperform other local trial fields.

Chapter 4

A Two-Level Domain Decomposition Method

4.1 Introduction

The Multiscale Spectral Generalized Finite Element Method (MS-GFEM) developed in [6] involves computing local solutions on every patch of the partition as well as constructing and solving large local spectral problems. In this chapter we show that these local computations may be leveraged through a two-level domain decomposition procedure allowing for the mitigation of some of these expensive upfront costs. We provide a near-exponential convergence estimate. In the prior chapter we showed that the method converges exponentially with respect to using more local basis functions. With this iterative procedure, we propose using fewer local basis functions for the global solve and iterate the solution to obtain a geometric convergence rate based on the exponential convergence properties of the local basis functions. The need for fewer local basis functions will allow for savings on the local subdomains through ending iterative computations of the spectral problems sooner, and on the global domain through a smaller global stiffness matrix.

4.2 Problem Formulation

We use the same problem formulation as in chapter 3 using pure Neumann boundary conditions. We briefly restate the key components here for convenience. Let $\Omega \subset \mathbb{R}^2$, be a bounded domain with piecewise smooth boundary. We study the following linear elliptic equation in which we seek $u \in H^1(\Omega)$ satisfying

$$\begin{cases} -\operatorname{div}(A(x)\nabla u(x)) = f(x) \text{ on } \Omega \\ \qquad n \cdot A(x)\nabla u(x) = g(x) \text{ on } \partial\Omega \end{cases} \tag{4.1}$$

where $f \in (H^1(\Omega))^*$, the dual space of $H^1(\Omega)$, and $g \in H^{-1/2}(\partial\Omega)$. Here A has coefficients in $L^\infty(\Omega)$. In weak form, $u \in H^1(\Omega)$ satisfies

$$(u, v)_{\mathcal{E}(\Omega)} = \int_\Omega fv \, dx + \int_{\partial\Omega} gv \, ds \tag{4.2}$$

for all $v \in H^1(\Omega)$. We fix a covering $\{\omega_i\}_{i=1}^N$, a partition of unity $\{\phi_i\}_{i=1}^N$ subordinate to the covering, and an expanded covering $\{\omega_i^*\}_{i=1}^N$ with $\omega_i \subset \omega_i^*$. The local particular solution χ_i on interior patches $\partial\omega_i^* \cap \partial\Omega = \emptyset$ satisfies

$$\begin{cases} -\operatorname{div}(A\nabla\chi_i) = f \text{ on } \omega_i^* \\ \chi_i = 0 \text{ on } \partial\omega_i^* \end{cases} \tag{4.3}$$

and on boundary patches $\partial\omega_i^* \cap \partial\Omega \neq \emptyset$ satisfies

$$\begin{cases} -\operatorname{div}(A\nabla\chi_i) = f \text{ on } \omega_i^* \\ n \cdot A\nabla\chi_i = g \text{ on } \partial\omega_i^* \cap \partial\Omega = \Gamma_i^N \\ \chi_i = 0 \text{ on } \partial\omega_i^* \cap \Omega = \Gamma_i^D. \end{cases} \tag{4.4}$$

The MS-GFEM problem is posed over the convex space $K_0^N = V^N + u_0^F$, where $u_0^F = \sum_{i=1}^N \phi_i\chi_i$ and $V^N = \{\sum_{i=1}^N \phi_i\xi_i : \xi_i \in V_{\omega_i^*}^{m_i}\}$. The problem is to find $u_0^G \in V^N$ such that

$$(u_0^G, v)_{\mathcal{E}(\Omega)} = \int_\Omega fv \, dx - (u_0^F, v)_{\mathcal{E}(\Omega)} \text{ for all } v \in V^N. \tag{4.5}$$

We write the initial solution as $u_0 = u_0^G + u_0^F \in K_0^N$.

We note that with $\xi_i \in H_A(\omega_i^*)$ for interior patches and $\xi_i \in H_{A,0}(\omega_i^*)$ for boundary patches, where

$$H_A(\omega_i^*) = \{u \in H^1(\omega_i^*) : (u, v)_{\mathcal{E}(\omega_i^*)} = 0 \text{ for all } v \in H_0^1(\omega_i^*)\} \tag{4.6}$$

and

$$H_{A,0}(\omega_i^*) = \{u \in H_A(\omega_i^*) : n \cdot A\nabla u = 0 \text{ on } \partial\omega_i^* \cap \partial\Omega\}. \tag{4.7}$$

We define the solution operator of (4.5) as $\mathcal{A}_C$. In implementation of MS-GFEM, this would be the global stiffness matrix with entires $(\phi_i\xi_i^q, \phi_j\xi_j^r)_{\mathcal{E}(\Omega)}$. Forming this matrix involves building the approximation space $H_{\mathbb{A}}(\omega_i^*)$ and solving the associated spectral problem over each ω_i^*, and then computing cross products $(u,v)_{\mathcal{E}(\Omega)}$ to fill in the stiffness matrix. We seek to leverage all this work that goes into forming $\mathcal{A}_C$ by iterating the right hand side of the MS-GFEM problem (4.5). This is done by iterating u^F, which we will identify as the fine grid correction. Since MS-GFEM provides excellent approximation of the $\mathbb{A}$-harmonic part of the solution, u^G, we improve the fine grid part of the solution with this information and resolve (4.5) to create a coarse grid correction. Algorithm 4.3 assumes u_0^F is given. The find grid smoother, $\mathcal{A}_{F_i}$, could be given by any typical finite element stiffness matrix, for example. In this method, we solve for the coarse grid correction u_0^G given by

$$(u_0^G, v)_{\mathcal{E}(\Omega)} = (f,v)_{L^2(\Omega)} - \mathcal{L}_C(u_0^F)v \text{ for } v \in V^N, \tag{4.8}$$

which is the Galerkin formulation of the MS-GFEM problem.

4.3 Domain Decomposition Method Preliminaries

In this section we introduce the two-level method based on MS-GFEM. We begin by defining the A-harmonic projection maps.

On interior patches we have the decomposition

$$H^1(\omega_i^*) = H_A(\omega_i^*) \oplus H_0^1(\omega_i^*) \tag{4.9}$$

and on boundary patches we have

$$H^1(\omega_i^*) = H_{A,0}(\omega_i^*) \oplus H_{A,0}^{\perp}(\omega_i^*) = H_{A,0}(\omega_i^*) \oplus H_{\Gamma_i^D}^1(\omega_i^*) \tag{4.10}$$

where

$$H_{\Gamma_i^D}^1(\omega_i^*) = \{v \in H^1(\omega_i^*) : v = 0 \text{ on } \Gamma_i^D\} \tag{4.11}$$

and orthogonality is with respect to the energy inner product defined as

$$(u, v)_{\mathcal{E}(\omega_i^*)} = \int_{\mathcal{E}(\omega_i^*)} A\nabla u \cdot \nabla v \, dx. \tag{4.12}$$

The orthogonal projection onto $H_A(\omega_i^*)$ for an interior patch ω_i^* is written as

$$\mathbb{P}_i^A : H^1(\Omega) \to H_A(\omega_i^*) \tag{4.13}$$

where $v = \mathbb{P}_i^A u$ is the function satisfying

$$\begin{cases} -\operatorname{div}(A\nabla v) = 0 \text{ on } \omega_i^* \\ \qquad\qquad v = u \text{ on } \partial\omega_i^*. \end{cases} \tag{4.14}$$

The orthogonal projection onto $H_{A,0}(\omega_i^*)$ for a boundary patch ω_i^* is written as

$$\mathbb{P}_i^{A,0} : H^1(\Omega) \to H_{A,0}(\omega_i^*) \tag{4.15}$$

where $v = \mathbb{P}_i^{A,0} u$ is the function satisfying

$$\begin{cases} -\operatorname{div}(A\nabla v) = 0 \text{ on } \omega_i^* \\ \quad n \cdot A\nabla v = 0 \text{ on } \partial\omega_i^* \cap \partial\Omega = \Gamma_i^N \\ \qquad\qquad v = u \text{ on } \partial\omega_i^* \cap \Omega = \Gamma_i^D. \end{cases} \tag{4.16}$$

After an initial application of the MS-GFEM algorithm we have the initial solution given by $u_0 = u_0^G + u_0^F = K_0^N$. The solution u_0 may be written as

$$u_0 = \sum_{i=1}^{N} \phi_i \xi_i^0 + \sum_{i=1}^{N} \phi_i \chi_i \tag{4.17}$$

Applying the A-harmonic projection maps to the initial solution, we define

$$u_1^F = \sum_{i \in I} \phi_i(\chi_i + \mathbb{P}_i^A u_0) + \sum_{i \in B} \phi_i(\chi_i + \mathbb{P}_i^{A,0} u_0) \tag{4.18}$$

where I is the set of indices such that ω_i^* is an interior patch, and B the the set of indices corresponding to boundary patches.

We define the convex space $K_1^N = V^N + u_1^F$ and solve for $u_1^G \in V^N$ satisfying the Galerkin formulation

$$(u_1^G, v)_{\mathcal{E}(\Omega)} = \int_\Omega f v \, dx - (u_1^F, v)_{\mathcal{E}(\Omega)} \text{ for all } v \in V^N. \tag{4.19}$$

Then the iterated solution to (4.1) is $u_1 = u_1^G + u_1^F$ and can be written as

$$u_1 = \sum_{i=1}^N \phi_i \xi_i^1 + \sum_{i \in I} \phi_i (\chi_i + \mathbb{P}_i^A u_0) + \sum_{i \in B} \phi_i (\chi_i + \mathbb{P}_i^{A,0} u_0). \tag{4.20}$$

Upon iterating we define the space $K^N = V^N + u_k^F$ where

$$u_k^F = \sum_{i=1}^N \phi_i \chi_i + \sum_{i \in I} \phi_i \mathbb{P}^A u_{k-1} + \sum_{i \in B} \phi_i \mathbb{P}^{A,0} u_{k-1} \tag{4.21}$$

and we arrive at the algorithm

Algorithm 4.1. *Initialize $u_0 = u_0^G + u_0^F$ as defined above.*

1. *Define $u_k^F = \sum_{i=1}^N \phi_i \chi_i + \sum_{i \in I} \phi_i \mathbb{P}^A u_{k-1} + \sum_{i \in B} \phi_i \mathbb{P}^{A,0} u_{k-1}$*

2. *Solve for u_k^G satisfying*

$$(u_k^G, v)_{\mathcal{E}(\Omega)} = \int_\Omega f v \, dx - (u_k^F, v)_{\mathcal{E}(\Omega)} \text{ for all } v \in V^N. \tag{4.22}$$

   where $u_k^G = \sum_{i=1}^N \phi_i \xi_i^k$ for $\xi_i^k \in V_{\omega_i^*}^{m_i}$.

3. *Set $u_k = u_k^G + u_k^F = \sum_{i=1}^N \phi_i \xi_i^k + \sum_{i \in I} \phi_i (\chi_i + \mathbb{P}_i^A u_{k-1}) + \sum_{i \in B} \phi_i (\chi_i + \mathbb{P}_i^{A,0} u_{k-1})$.*

Theorem 4.2. *Using the two-level MS-GFEM algorithm, we have the a priori error estimate for the k-*th *step*

$$\|u - u_k\|_{\mathcal{E}(\Omega)}^2 \leq \left(C e^{-m^{1/(1+d)}} \right)^{k+1} \|u\|_{\mathcal{E}(\Omega)}^2$$

with C depending on the number of patches, their size, and the chosen partition of unity. It is assumed here that the local particular solutions χ_i are given exactly. The dimension $d = 2, 3$ for $\Omega \subset \mathbb{R}^d$.

Proof. By using (3.26) from Theorem 3.2 and the fact that $\mathbb{P}_i u = u - \chi_i$, we have for the first iteration u_1

$$\begin{aligned}
\|u - u_1\|^2_{\mathcal{E}(\Omega)} &\leq C \sum_{i=1}^{N} \|u - \left(\xi_i^1 + \chi_i + \mathbb{P}_i u_0\right)\|^2_{\mathcal{E}(\omega_i^*)} \\
&= C \sum_{i=1}^{N} \|\left(u - \chi_i - \mathbb{P}_i u_0^G\right) - \xi_i^1\|^2_{\mathcal{E}(\omega_i^*)} \\
&\leq C e^{-m^{1/(1+d)}} \sum_{i=1}^{N} \|\mathbb{P}_i \left(u - u_0^G\right)\|^2_{\mathcal{E}(\omega_i^*)} \\
&= C e^{-m^{1/(1+d)}} \|\left(u - u_0^G\right)\|^2_{\mathcal{E}(\Omega)} \\
&\leq \left(C e^{-m^{1/(1+d)}}\right)^2 \|u\|^2_{\mathcal{E}(\Omega)}
\end{aligned} \tag{4.23}$$

Here C is used to absorb all constants at each step. Usage of (3.26) is justified since u_0^G is the solution to the Galerkin formulation (3.26), implying that

$$\|u_A - u_1^G\|_{\mathcal{E}(\Omega)} = \inf_{u^G \in V^N} \|u_A - u^G\|_{\mathcal{E}(\Omega)}, \tag{4.24}$$

where $u_A \in H^1(\Omega)$ is the exact solution of (4.19). The k-th step follows inductively.

□

4.4 Domain Decomposition Method

Having established the near-exponential convergence estimate of the method introduced in section 4.3, we proceed to translate the method into the standard parlance of domain decomposition methods. We state the updated algorithm then define the necessary terms.

Algorithm 4.3. *Let $u_0^F = \sum_{i=1}^{N} \phi_i \chi_i$ be the fine grid initialization with $\chi_i = \mathcal{A}_{F_i}^{-1} f$ for interior patches and $\chi_i = \tilde{\mathcal{A}}_{F_i}^{-1} f$ for boundary patches. Then the algorithm proceeds as*

1. *Solve $\mathcal{A}_C u_0^G = \mathcal{P} f - \mathcal{L}_C(u_0^F)$*

   Set $u_0 = u_0^G + u_0^F$ the 0-th *approximate solution*

2. *Solve* $u_k^F = u_{k-1} + \sum_{i\in I} \phi_i A_{F_i}^{-1}(f - L_{F_i}(u_{k-1})) + \sum_{i\in B} \phi_i \tilde{A}_{F_i}^{-1}(f - \tilde{L}_{F_i}(u_{k-1}))$
Solve $\mathcal{A}_C u_k^G = \mathcal{P}f - \mathcal{L}_C(u_k^F)$

3. *Set* $u_k = u_k^G + u_k^F$ *the* k-th *approximate solution.*

In this algorithm we have the fine grid initialization given by u_0^F, composed of the local particular solutions. The coarse grid correction is given by u_0^G, the global contribution to the solution consisting of the optimal local basis functions. The fine grid smoother is given by $\mathcal{A}_{F_i}$ and $\tilde{\mathcal{A}}_{F_i}$. The restriction operator taking the coarse grid of patches to the fine grid on ω_i is $\mathcal{L}_{F_i}$. The prolongation operator is given by $\mathcal{L}_C$ which takes the fine grid to the coarse grid. Lastly the operator $\mathcal{P}$ takes elements of the dual to the solution space on the fine grid to the dual of the solution space on the coarse grid. We define these operators rigorously below.

The coarse grid solution operator is defined as $\mathcal{A}_C : V^N \to (V^N)^*$ such that for $u \in V^N$

$$\mathcal{A}_C(u) = (u, \cdot)_{\mathcal{E}(\Omega)} \tag{4.25}$$

is the operator acting on V^N. The existence of $\mathcal{A}_C$ and its inverse is guaranteed by the Lax-Milgram theorem.

The restriction operator $\mathcal{L}_C : H^1(\Omega) \to (V^N)^*$ is defined such that for $u \in H^1(\Omega)$

$$\mathcal{L}_C(u) = (u, \cdot)_{\mathcal{E}(\Omega)} \tag{4.26}$$

is the linear functional acting on V^N.

The operator $\mathcal{P} : (H^1(\Omega))^* \to (V^N)^*$ is defined such that for $f \in (H^1(\Omega))^*$

$$\mathcal{P}f = (f, \cdot)_{L^2(\Omega)} \tag{4.27}$$

is the linear functional acting on V^N.

Substituting (4.25), (4.26), and (4.27) into Algorithm 4.1 gives the coarse grid correction at the k-th step as

$$\mathcal{A}_C(u_k^G) = \mathcal{P}f - \mathcal{L}_C(u_k^F). \tag{4.28}$$

We define the prolongation operators and fine grid smoothers in two cases, first over interior patches then boundary patches.

4.4.1 Interior Patches

Using the decomposition (4.9) for interior patches we define the orthogonal projection

$$\mathbb{P}_i^0 : H^1(\Omega) \to H_0^1(\omega_i^*) \tag{4.29}$$

such that the identity on $H^1(\Omega)$ is written $\mathcal{I} = \mathbb{P}_i^A + \mathbb{P}_i^0$. Then we have for $u \in H^1(\Omega)$ that $\mathbb{P}_i^0 u = w \in H_0^1(\omega_i^*)$ is the function satisfying

$$\begin{cases} -\operatorname{div}(A\nabla w) = -\operatorname{div}(A\nabla u) \text{ on } \omega_i^* \\ \qquad\qquad w = 0 \text{ on } \partial\omega_i^*. \end{cases} \tag{4.30}$$

The weak formulation of (4.30) is given for $w \in H_0^1(\omega_i^*)$ by

$$(w, v)_{\mathcal{E}(\omega_i^*)} = (u, v)_{\mathcal{E}(\omega_i^*)} \tag{4.31}$$

for all $v \in H_0^1(\omega_i^*)$. Using the left hand side of (4.31) the fine grid smoother is defined as

$$\mathcal{A}_{F_i}(w) = (w, \cdot)_{\mathcal{E}(\omega_i^*)} \tag{4.32}$$

acting on $H_0^1(\omega_i^*)$ where

$$\mathcal{A}_{F_i} : H_0^1(\omega_i^*) \to (H_0^1(\omega_i^*))^* \tag{4.33}$$

with $(H_0^1(\omega_i^*))^*$ the dual space of $H_0^1(\omega_i^*)$. The right hand side of (4.31) gives the prolongation operator as

$$\mathcal{L}_{F_i}(u) = (u, \cdot)_{\mathcal{E}(\omega_i^*)} \tag{4.34}$$

acting on $H_0^1(\Omega)$ such that

$$\mathcal{L}_{F_i} : H^1(\Omega) \to (H_0^1(\omega_i^*))^*. \tag{4.35}$$

Then (4.31) becomes

$$\mathcal{A}_{F_i}(w) = \mathcal{L}_{F_i}(u) \tag{4.36}$$

and $\mathbb{P}_i^0 = w = \mathcal{A}_{F_i}^{-1}\mathcal{L}_{F_i}(u)$. We compute $\mathbb{P}_i^A$ as

$$\mathbb{P}_i^A u = (\mathcal{I} - \mathbb{P}_i^0)u \tag{4.37}$$

for any $u \in H^1(\Omega)$, from which it follows that

$$P_i^A u = (\mathcal{I} - \mathcal{A}_{F_i}^{-1}\mathcal{L}_{F_i})u. \tag{4.38}$$

We see from (4.3) that $\mathcal{A}_{F_i}\chi_i = \mathcal{L}_{F_i}\chi_i = \mathcal{L}_{F_i}u = f$, thus

$$\chi_i = \mathcal{A}_{F_i}^{-1} f. \tag{4.39}$$

Substituting (4.39) and (4.37) into (4.21) gives

$$u_k^F = \sum_{i\in I} \phi_i \mathcal{A}_{F_i}^{-1}(f - \mathcal{L}_{F_i}(u_{k-1})) + \sum_{i\in B} \phi_i(\chi_i + \mathbb{P}_i^{A,0} u_{k-1}) + \sum_{i\in I} \phi_i u_{k-1}. \tag{4.40}$$

4.4.2 Boundary Patches

We follow the exact same lines as for interior patches except now we use the decomposition (4.10) and define the projection

$$\mathbb{P}_i^{0,\Gamma} : H^1(\Omega) \to H^1_{\Gamma_i^D}(\omega_i^*) \tag{4.41}$$

such that the identity on $H^1(\Omega)$ is written $\mathcal{I} = \mathbb{P}_i^{A,0} + \mathbb{P}_i^{0,\Gamma}$. Then we have for $u \in H^1(\Omega)$ that $\mathbb{P}_i^{0,\Gamma} u = w \in H^1_{\Gamma_i^D}(\omega_i^*)$ is the function satisfying

$$\begin{cases} -\operatorname{div}(A\nabla w) = -\operatorname{div}(A\nabla u) \text{ on } \omega_i^* \\ \qquad\qquad w = 0 \text{ on } \partial\omega_i^* \cap \Omega = \Gamma_i^D \\ n \cdot A\nabla w = n \cdot A\nabla u \text{ on } \partial\omega_i^* \cap \partial\Omega = \Gamma_i^N. \end{cases} \tag{4.42}$$

The weak formulation of (4.42) is given for $w \in H^1_{\Gamma_i^D}(\omega_i^*)$ by

$$(w, v)_{\mathcal{E}(\omega_i^*)} = (u, v)_{\mathcal{E}(\omega_i^*)} \tag{4.43}$$

for all $v \in H^1_{\Gamma_i^D}(\omega_i^*)$. Using the left hand side of (4.31) the fine grid smoother is defined as

$$\tilde{\mathcal{A}}_{F_i}(w) = (w, \cdot)_{\mathcal{E}(\omega_i^*)} \tag{4.44}$$

acting on $H^1_{\Gamma_i^D}(\omega_i^*)$ where

$$\tilde{\mathcal{A}}_{F_i} : H^1_{\Gamma_i^D}(\omega_i^*) \to (H^1_{\Gamma_i^D}(\omega_i^*))^*. \tag{4.45}$$

The right hand side of (4.43) gives the prolongation operator as

$$\tilde{\mathcal{L}}_{F_i}(u) = (u, \cdot)_{\mathcal{E}(\omega_i^*)} \tag{4.46}$$

acting on $H^1_{\Gamma_i^D}(\Omega)$ such that

$$\tilde{\mathcal{L}}_{F_i} : H^1(\Omega) \to (H^1_{\Gamma_i^D}(\omega_i^*))^*. \tag{4.47}$$

Then (4.43) becomes

$$\tilde{\mathcal{A}}_{F_i}(w) = \tilde{\mathcal{L}}_{F_i}(u) \tag{4.48}$$

and $\mathbb{P}_i^{0,\Gamma} = w = \tilde{\mathcal{A}}_{F_i}^{-1}\tilde{\mathcal{L}}_{F_i}(u)$. We compute $\mathbb{P}_i^{A,0}$ as

$$\mathbb{P}_i^{A,0}u = (\mathcal{I} - \mathbb{P}_i^{0,\Gamma})u \tag{4.49}$$

for any $u \in H^1(\Omega)$, from which it follows that

$$\mathbb{P}_i^{A}u = (\mathcal{I} - \tilde{\mathcal{A}}_{F_i}^{-1}\tilde{\mathcal{L}}_{F_i})u. \tag{4.50}$$

We see from (4.4) that $\tilde{\mathcal{A}}_{F_i}\chi_i = \tilde{\mathcal{L}}_{F_i}\chi_i = \tilde{\mathcal{L}}_{F_i}u = f$, thus

$$\chi_i = \tilde{\mathcal{A}}_{F_i}^{-1}f. \tag{4.51}$$

Substituting (4.51) and (4.49) into (4.40) gives

$$u_k^F = u_{k-1} + \sum_{i\in I} \phi_i \mathcal{A}_{F_i}^{-1}(f - \mathcal{L}_{F_i}(u_{k-1})) + \sum_{i\in B} \phi_i \tilde{\mathcal{A}}_{F_i}^{-1}(f - \tilde{\mathcal{L}}_{F_i}(u_{k-1})) \tag{4.52}$$

where we have used $\sum_{i=1}^N \phi_i = 1$ to recover u_{k-1}. With (4.52) substituted into Algorithm 4.1 we recover the fine grid smoothing of Algorithm 4.3 and the domain decomposition method is fully defined.

4.5 Conclusion

An iterative method based on MS-GFEM was presented and shown to converge with a rate related to the near-exponential convergence bounds provided by MS-GFEM. The iterative method utilized the optimal local spectral functions by projecting on this part of the iterated solution to the right hand side of the solution by adding it to u^F and then improving the residual on the coarse grid with the spectral functions again. The method was reformulated into a domain decomposition method in which the necessary operators for switching between the two levels of the method were defined.

We finish by observing that this method can, in principle, be applied to any GFEM method similar to MS-GFEM in the following sense. For any GFEM approximation space $V^N \subset \sum_{i=1}^N \phi_i H_{\mathbb{A}}(\omega_i^*)$, if the a priori error estimate

$$\|\mathbb{P}_i u - \xi\|_{\mathcal{E}(\omega_i)} \leq \tau C \|u\|_{\mathcal{E}(\omega_i^*)} \tag{4.53}$$

holds for $\tau C < 1$, $\xi \in V_{\omega_i^*}^m$, $i = 1, \ldots, N$, then we can apply this two-level method.

The method can be applied in any setting in which the following two properties hold. First, the decomposition of the local solution spaces must be given by $H^1(\omega_i^*) = H_{\mathbb{A}}(\omega_i^*) \oplus H_0^1(\omega_i^*)$, where orthogonality is with respect to the energy inner product. Secondly, the approximation property (4.53) must hold for each of the local bases in $H_{\mathbb{A}}(\omega_i^*)$. Therefore, if it is desirable to use another class of

local basis functions besides the spectral functions provided by MS-GFEM, then this two-level method will be adaptable to the other proposed class of functions provided that it has a favorable oversampling approximation property similar to the local spectral basis.

References

[1] B. Alali, and R. Lipton, Optimal lower bounds on local stress inside random media. *SIAM Journal On Applied Mathematics*, 70, 2009, 1260–1282.

[2] I. Babuška, U. Banerjee, J.E. Osborn, Survey of meshless and generalized finite element methods: a unified approach, *Acta Numer.*, 12, 2003, 1–125.

[3] I. Babuška, G. Caloz, and J. E. Osborn, Special finite element methods for a class of second order elliptic problems with rough coefficients, *SIAM J. Numer. Anal.*, 31, 1994, 945–981.

[4] T. Belytschko, R. Gracie, Giulio Ventura, A review of extended/generalized finite element methods for material modeling, *Modeling Simul. Mater. Sci. Eng.*, 17, 2009, 1–24.

[5] I. Babuška, X. Huang, and R. Lipton, Machine computation using the exponentially convergent multiscale spectral generalized finite element method, *ESAIM: Mathematical modeling and Numerical Analysis*, 48, 2014, 493–515.

[6] I. Babuška, and R. Lipton, Optimal local approximation spaces for generalized finite element methods with application to multiscale problems, *Multiscale Model. and Simul., SIAM*, 9, 2011, 373–406.

[7] I. Babuška, R. Lipton, and M. Stuebner, The Penetration Function and its Application to Microscale Problems, *BIT Numer Math*, 48, 2008, 167–187.

[8] I. Babuška and J. Melenk, The partition of unity finite element method, *Internat. J. Numer. Methods Engrg.,* 40, 1997, 727–758.

[9] L. Berlyand and H. Owhadi. Flux norm approach to finite dimensional homogenization approximations with non-separated scales and high contrast, *Archive for Rational Mechanics and Analysis,* 198, 2010, 677–721.

[10] Y. Chen and R. Lipton, Optimal lower bounds on the local stress inside random thermoelastic composites, *Acta Mechanica*, 213, 2010, 97-109.

[11] C.-C. Chu, I. G. Graham and T.-Y. Hou, A new multiscale finite element method for high-contrast elliptic interface problems, *Math. Comp.*, 79, 2010, 1915–1955.

[12] B. Dacorogna, Direct Methods in the Calculus of Variations, Springer-Verlag, Berlin, 1989.

[13] Y. Efendiev and J. Galvis, Domain decomposition preconditioners for multiscale flows in high-contrast media, *Multiscale Modeling and Simulation*, 8, 2010, 1461–1483.

[14] R.G. Ghanem and P.D. Spanos, Stochastic Finite Elements: A Spectral Approach, Springer-Verlag, New York, 1991.

[15] V. Girault and P.-A. Raviart, Finite Element Approximation of the Navier-Stokes Equation, Lecture Notes in Mathematics, Springer-Verlag, New York, 1979.

[16] M. Griebel, M.A. Schweitzer, A Particle-Partition of Unity Method Part VII: Adaptivity, Meshfree Methods for Partial Differential Equations III, *Lecture Notes in Computational Science and Engineering*, Springer, 57, 2007, 121–147.

[17] C. O. Horgan, Saint-Venant end effects in composites, *J. Composite Materials*, 16, 1982, 411–422.

[18] T.J.R. Hughes, The Finite Element Method, Dover Publications, Mineola, 2000.

[19] Intel(R) Math Kernel Library 11.1 for Linux*.

[20] R. Lipton, Assessment of the local stress state through macroscopic variables, *Philosophical Transactions Mathematical, Physical and Engineering Sciences*, 361, 2003, 921–946.

[21] R. Lipton, P. Sinz, M. Stuebner, Uncertain loading and quantifying maximum energy concentration within composite structures, *Journal of Computational Physics*, 325, 2016, 38–52.

[22] R. Lipton and M. Stuebner, Inverse homogenization and design of microstructure for pointwise stress control, *The Quarterly Journal of Mechanics and Applied Mathematics*, 59, 2006, 139–161.

[23] R. Lipton, R. Viator, Bloch waves in crystals and periodic high contrast media, *ESAIM: Mathematical Modeling and Numerical Analysis*, 51, 2017, 889–918.

[24] R. Lipton, R. Viator, Creating Band Gaps in Periodic Media, To appear in *Multiscale Modeling and Simulation*, 2017.

[25] A. E. H. Love, A Treatise on the Mathematical Theory of Elasticity, Cambridge University Press, 1927.

[26] P. Maremonti and R. Russo, On the Von-Mises-Sternberg version of St Venant's principle in plane linear elastostatics, Arch. Rational Mech Anal., 128, 1994, 207–221.

[27] J.M. Melenk, I. Babuška, The partition of unity finite element method: basic theory and applications, *Comput. Methods Appl. Mech. Eng.*, 39, 1996, 289–314.

[28] A. Pinkus, n-Widths in Approximation Theory, Springer-Verlag, Berlin, 1985.

[29] A. J. C. B. Saint-Venant, Memoire sur la Torsion des Prismes, Mem. Divers Savants, 14, 1885, 233–560.

[30] M.A. Schweitzer, S. Wu, Evaluation of local multiscale approximation spaces for partition of unity methods, preprint, 2017.

[31] B. Smith, P. Bjørstad, W. Gropp, Domain Decomposition: Parallel Multilevel Methods for Elliptic Partial Differential Equations, Cambridge University Press, Cambridge, 2004.

[32] T. Strouboulis, I. Babuška, and K. Copps, The design and analysis of the generalized finite element method, *Comput. Methods Appl. Mech. Engrg.,* 181, 2001, 43–69.

[33] T. Strouboulis, L. Zhang, I. Babuška, Generalized finite element method using mesh-based handbooks: application to problems in domains with many voids, *Comput. Methods Appl. Mech. Engrg.*, 192, 2003, 3109-3161.

[34] L. Tong and C. Soutis, Recent Advances in Structural Joints and Repairs for Composite Materials, Kluwer Academic Publishers, Dordrecht, The Netherlands, 2003.

[35] R. von Mises, On Saint-Venant's Principle, *Bull. AMS*, 51, 1945, 555–562.

[36] J. Xu, Iterative Methods by Space Decomposition and Subspace Correction, *SIAM Review*, 34, 1992, 581–613.

Vita

Paul Sinz was born in Alamo, California. He finished his undergraduate studies in Mathematics with a minor in Physics at California Polytechnic State University in San Luis Obispo in 2010. He earned a master of science in Mathematics from Louisiana State University in 2011. He is currently a candidate for the degree of Doctor of Philosophy in Mathematics at Louisiana State University which will be awarded in August 2017.